Conf-730941--1

MASTER

CALCULATIONS RELATED TO THE APPLICATION OF NEUTRONS, PROTONS, NEGATIVELY CHARGED PIONS, AND HEAVY IONS IN CANCER RADIOTHERAPY*

R. G. Alsmiller, Jr.
Oak Ridge National Laboratory
Oak Ridge, Tennessee, 37830

Abstract

This report describes some of the most significant aspects of the research which has been conducted during the past year (September 1, 1972 to August 31, 1973) on the NSF/RANN-supported projects: A Comparative Study of the Use of Photons, Neutrons, Protons, Negatively Charged Pions, and Heavy Ions in Cancer Radiotherapy and Calculations for Cancer Radiotherapy with Negatively Charged Pions. The report contains the information presented to the Grantees Conference on Instrumentation Technology held by the National Science Foundation on September 25 and 26, 1973 at Washington, D. C. as part of the RANN program.

---

*This research is funded by the National Science Foundation, Order NSF/RANN AG-399, under Union Carbide Corporation's contract with the U. S. Atomic Energy Commission.

DISTRIBUTION OF THIS DOCUMENT IS UNLIMITED

A COMPARATIVE STUDY OF THE USE OF PHOTONS, NEUTRONS, PROTONS, NEGATIVELY CHARGED PIONS, AND HEAVY IONS IN CANCER RADIOTHERAPY

SENIOR INVESTIGATOR

R. G. Alsmiller, Jr.

Neutron Physics Division

COINVESTIGATORS

T. W. Armstrong
H. W. Bertini
G. T. Chapman
T. A. Gabriel
R. T. Santoro

Neutron Physics Division

J. Barish
K. C. Chandler
O. W. Hermann
N. M. Larson

Computer Sciences Division

CALCULATIONS FOR CANCER RADIOTHERAPY WITH NEGATIVELY CHARGED PIONS

SENIOR INVESTIGATOR

R. G. Alsmiller, Jr.

Neutron Physics Division

COINVESTIGATORS

T. W. Armstrong
G. T. Chapman
R. T. Santoro

Neutron Physics Division

R. N. Hamm
J. E. Turner
H. A. Wright

Health Physics Division

V. E. Anderson
K. C. Chandler

Computer Sciences Division

I. INTRODUCTION

The potential advantages of using radiations other than photons (e.g., neutrons, protons, negatively charged pions, and heavy ions) in cancer radiotherapy have been recognized for some time, and radiobiological experiments and therapeutic exposures with these other types of radiation are being carried out or will be carried out in the near future.* The physical and biological properties of these new radiation modalities will of necessity be different from those of photons, and therefore considerable physical and biological data will be needed before the manner in which these new modalities can most effectively be used in radiotherapy can be determined. The primary objective of the two programs, "A Comparative Study of the Use of Photons, Neutrons, Protons, Negatively Charged Pions, and Heavy Ions in Cancer Radiotherapy" and "Calculations for Cancer Radiotherapy with Negatively Charged Pions," is to arrive at accurate and general calculational methods which may be used to provide these needed data for any of these new radiation modalities. In this report, some of the most significant results obtained as part of these programs during the past year are presented and discussed.

---

*See, for example, ref. 1 and the references given therein.

II. CALCULATIONAL METHODS

The basic transport codes and the theoretical models used to predict particle production from pion-nucleus, nucleon-nucleus, and alpha-particle-nucleus collisions were developed with AEC and NASA funding over the past several years. Some modifications have been made in the codes for the present application,[2] but the effort involved in making these modifications was small compared to the total effort required to produce the codes.

Most of the results presented in this report were obtained with the nucleon-meson transport code HETC.[3] This code utilizes Monte Carlo methods to simulate particle transport, charged-particle energy loss due to atomic excitation and ionization, multiple Coulomb scattering of incident charged particles, elastic and nonelastic neutron collisions, and nonelastic pion and proton collisions with nuclei other than hydrogen, elastic and nonelastic nucleon and pion collisions with hydrogen nuclei, pion and muon decay in flight and at rest, and negative-pion capture at rest. A complete description of the manner in which these physical processes are included in the code is given in refs. 3-8. This code in its published form is operable for incident neutrons, protons, and pions for all energies of interest in radiotherapy and is capable of treating very general source-geometry configurations including an essentially arbitrary phantom composition. This code has been used extensively to calculate the energy deposition in tissue by incident neutrons, protons, and charged pions,[3,4,6,7] and results obtained with the code have been shown to be in good agreement with experimental data.[9,10]

The code HETC as described in ref. 3 is not operable for incident alpha particles. A version of the code to treat the transport of alpha particles and the nuclear-reaction products produced by alpha-particle-nucleus nonelastic collisions and alpha-particle-hydrogen elastic and nonelastic collisions has recently been written[11,12] and was used here. A description of the nuclear-reaction models used in obtaining the results presented here for incident alpha particles is given in ref. 12. In general, the nuclear-reaction models used to describe particle production from alpha-particle-nucleus collisions are more approximate than the models used to describe particle production from nucleon-nucleus and pion-nucleus collisions, and therefore the results for incident alpha particles presented here must be considered to be more approximate than the results presented for the other incident particles.

Another computer code presently being used in carrying out some of the calculations for incident pions is PION-1.[13] This code utilizes Monte Carlo methods and in many respects is similar to HETC, but it is quite different in conception. HETC is written to be as general as possible and every effort is made to include in as much detail as possible all physical interactions. On the other hand, PION-1 is written to include only those physical interactions which are thought to be important in pion transport. PION-1 is capable of operating at all energies of interest in radiotherapy and is capable of treating quite general source-geometry configurations. At the present time, it is restricted to phantom compositions which contain only the elements H, C, N, and O. Calculations carried out with PION-1 have been compared with experimental data, and, in general, good agreement has been obtained.[13] Because of its greater generality, HETC requires somewhat more computer time for a given case (approximately a factor of four) than does PION-1, and thus where it is thought to be applicable PION-1 should be used.

To be most useful in radiotherapy, the physical data obtained from the computer codes must be utilized to predict biological effects. There is no completely acceptable theory for predicting biological effects from physical data, but the essential feature of the codes mentioned above is that they provide a complete description of the particle spectra, i.e., the types, energy distributions, and angular distributions, as a function of position in a phantom which is being irradiated, and this information is thought to be sufficient for predicting biological effects, at least on the cellular level.

With the physical data given by the codes, it is possible to compute the spatial dependence of the absorbed dose in various linear-energy-transfer (LET) intervals* and then apply LET-dependent weighting factors for biological damage to estimate the spatial dependence of biological effects. In subsequent sections of this report, LET spectra for various incident particles are presented, but no attempt is made to estimate biological effects by introducing LET-dependent weighting factors.

Another approach to estimating biological effects is to use the particle spectra provided by the codes in conjunction with cell-inactivation models, such as that recently developed by Katz *et al.*,[14-16] to obtain

---

*A detailed description of the manner in which LET spectra may be constructed from the data obtained from HETC is given in ref. 7.

spatially dependent cell-survival probabilities, oxygen enhancement ratios (OER's), and relative biological effectiveness (RBE). This approach is dependent upon the particular cell-inactivation model used, but it has the advantage that calculated results may be compared directly with experimental data on cell inactivation. Also in later sections of this report, calculated cell-survival probabilities, obtained by combining HETC data with the Katz model, are presented and compared with experimental data.*

At the present time, the calculational methods available for studying the use of heavy ions in cancer radiotherapy are very approximate. A major impediment to performing accurate calculations is the lack of information on particle production from high-energy heavy-nucleus, heavy-nucleus collisions. As part of the present programs, a theoretical model is being developed[17] to provide the type, energy distribution, and angular distribution of all of the particles produced in such collisions. In another section of this report, some of the results obtained with the model are presented and discussed.

---

*A detailed description of the manner in which cell-survival probabilities, OER's, and RBE's may be obtained using HETC results and the Katz model is given in ref. 7.

III. COMPARISON OF CALCULATED AND EXPERIMENTAL ABSORBED-DOSE DATA FOR NEUTRONS FROM 35-MeV ^{2}H ON Be INCIDENT ON A TISSUE-EQUIVALENT PHANTOM[a]

The neutron-energy distribution from 35-MeV ^{2}H on Be as measured by Theus *et al.*[18] at the Naval Research Laboratory is shown in Fig. 1. The solid line is a smooth curve through the measured values. The dashed line is an extrapolation since the measurements do not extend below 5 MeV.

Theus[19] has measured the absorbed dose as a function of depth along the axis of a tissue-equivalent phantom when the neutron spectrum shown in Fig. 1 is incident on the phantom. Measurements were carried out using a source-to-phantom distance of 125 cm and with several cylindrical collimators which produced fields of radius R at the front of the phantom. The experimental data for R values of 17, 13, 9, 5, and 3 cm are shown as solid lines in Fig. 2.

Calculated results obtained with HETC, using the same geometry and tissue-equivalent composition as those used in the experiment, are shown by the histogram values in Fig. 2. In carrying out the calculations, the energy distribution shown in Fig. 1 was used, the neutrons were assumed to be emitted isotropically from a point source, and perfect collimation was assumed. The radial intervals over which the calculations were averaged to obtain an estimate of the center-line absorbed dose are specified in the figure for each collimator size. The error bars shown on the histograms are statistical and represent one standard deviation.

---

[a] Work performed by R. G. Alsmiller, Jr., J. Barish, and K. C. Chandler.

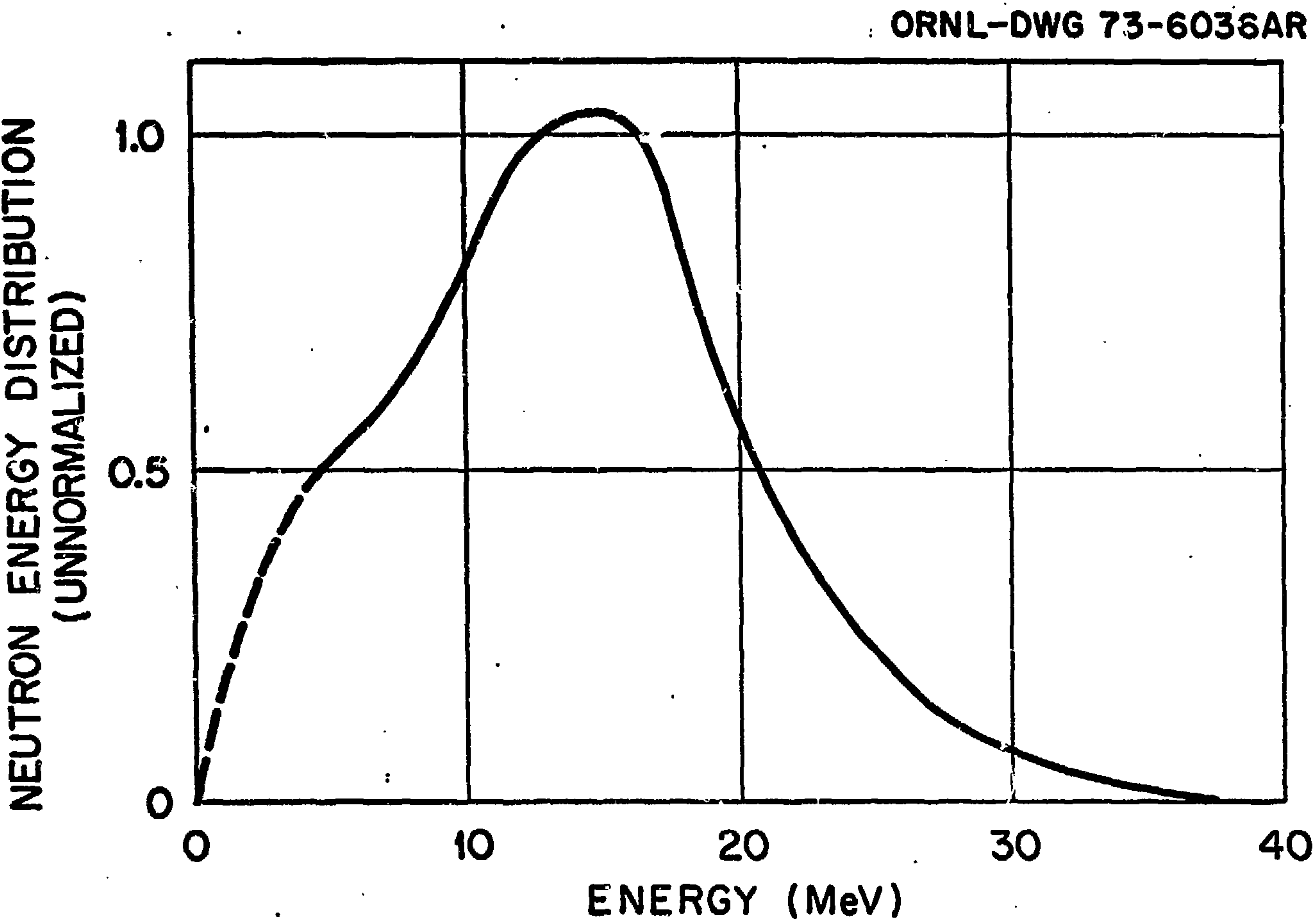

Fig. 1. Energy distribution of neutrons produced by 35-MeV ^{2}H on Be.

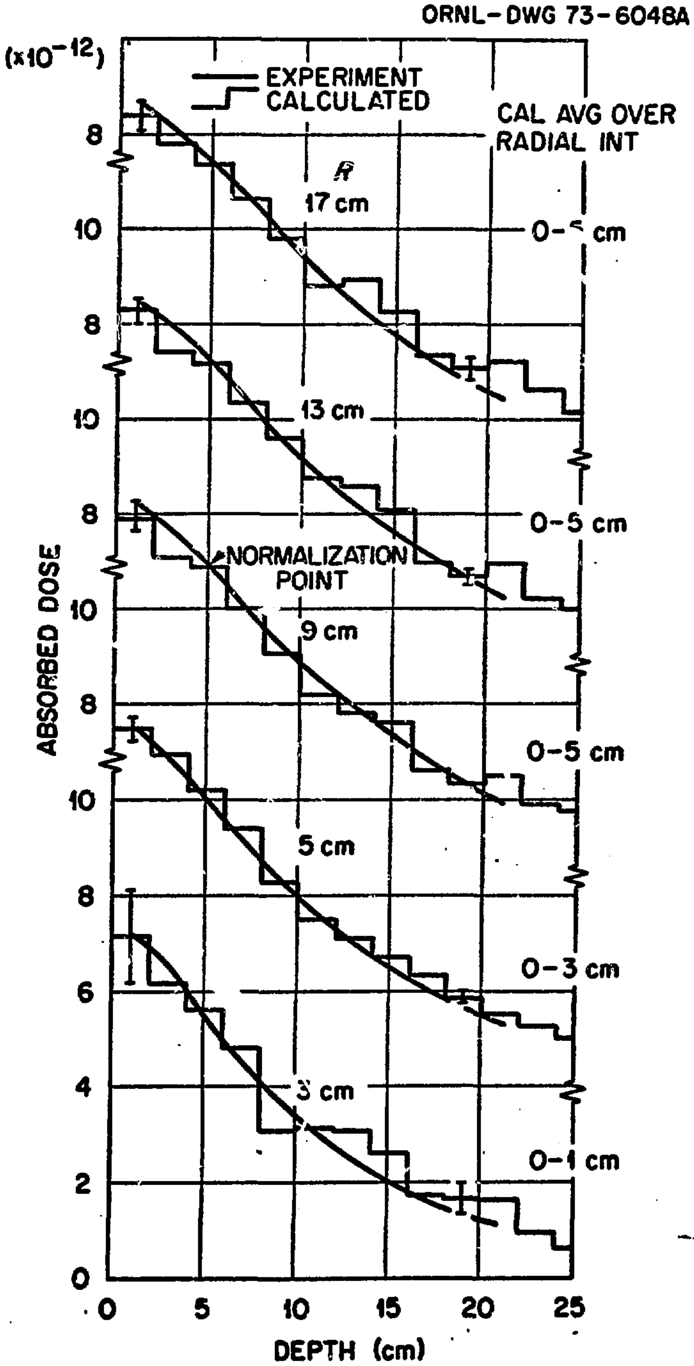

Fig. 2. Center-line absorbed dose vs depth for cylindrically collimated neutrons from 35-MeV ^{2}H on Be incident on a tissue-equivalent phantom. The units on the ordinate are arbitrary, but all data shown have the same normalization.

The absolute normalization of the experimental data is not known, but all of the data have the same normalization. To make the comparisons shown in Fig. 2, the normalization was established by making the calculated and experimental values agree at a depth of 5 cm for the R = 9 cm case. The agreement between the calculated and experimental data in all cases is very good.

Shown in Fig. 3 is a comparison between calculated and experimental absorbed-dose data as a function of distance from the beam center line for two depths when the spectrum shown in Fig. 1 is incident on a tissue-equivalent phantom. The experimental data are taken from the work of Todd *et al.*[20] In both the experimental measurements and the calculations, the source-to-phantom distance was 125 cm and the collimator produced a square field of 10 cm by 10 cm at the front of the phantom. The experimental data have been normalized to the calculated results at the point shown in the figure. The agreement between the calculated and experimental data is quite good at all distances from the center line and at both depths.

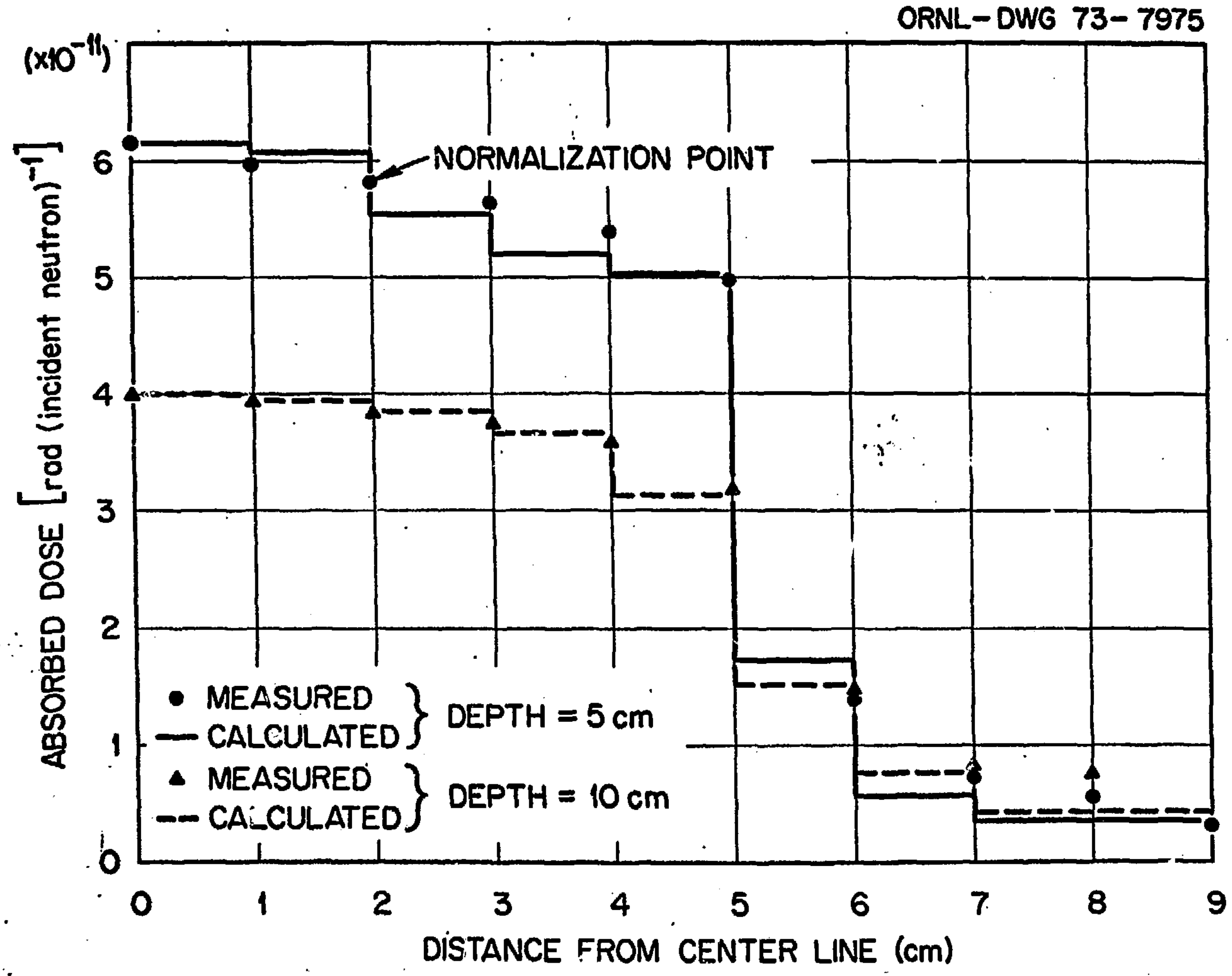

Fig. 3. Absorbed dose vs distance from the center line for neutrons from 35-MeV ^{2}H on Be incident on a tissue-equivalent phantom. The results shown are for a square field of 10 cm by 10 cm at the face of the phantom.

IV. COMPARISON OF CALCULATED AND MEASURED CELL-SURVIVAL PROBABILITIES*

Experimental data on the spatial dependence of cell-survival probabilities are not available at present for comparison with the calculated results. Cell-survival measurements have been made by Barendsen and Broerse[22,23] for a thin specimen of T-1 kidney cells exposed to 14-MeV neutrons, and in an experiment by Raju *et al.*[24] the survival of T-1 kidney cells has been measured at a single location in the stopping region of a pion beam. In this section, a comparison between calculated results and these experimental data is presented.

The code HETC[3] has been used to calculate the spectrum of charged particles produced by the interaction of 14-MeV neutrons with tissue nuclei (i.e., H, C, N, and O nuclei in the relative amounts found in tissue). These spectra were then used with the cell-inactivation model of Katz *et al.*[14] to compute cell-survival probabilities for T-1 kidney cells. The results of the calculations are shown in Fig. 4, together with the measurements of Barendsen and Broerse[22,23] for this case. Also shown in Fig. 4 are the results of Katz *et al.*[21] obtained using the charged-particle spectra of Caswell and Coyne[25] based on experimental cross-section data. Since the same radiosensitivity parameters were used in converting the calculated and experimental charged-particle spectra to cell-survival probabilities, any differences in Fig. 4 between the present calculations and the predictions of Katz *et al.* are due to differences in the spectra calculated with HETC and the experimental spectra used by Katz *et al.*

---

*This section is taken from the work of Armstrong and Chandler as reported in ref. 7.

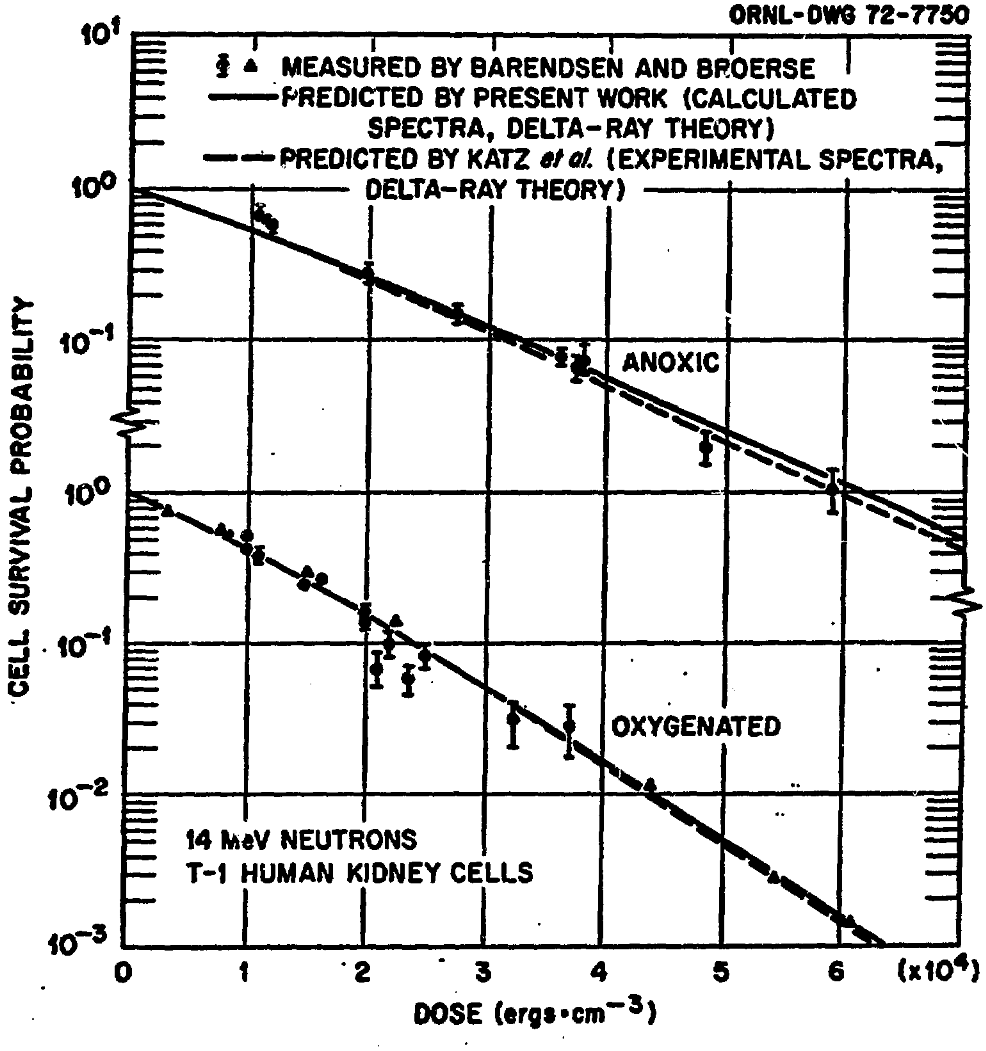

Fig. 4. Cell-survival probability vs absorbed dose for T-1 kidney cells irradiated by 14-MeV neutrons.

The measurements of Raju *et al.*[24] were made by placing T-1 kidney cells in the peak dose region of a contaminated pion beam (65% pions, 10% muons, 25% electrons) having a mean pion range of ≈ 23 g cm^{-2} in lucite. The experimental data, Fig. 5, show considerable spread because the experiment had to be performed using a low-intensity beam. Also shown in Fig. 5 is the calculated average cell survival in the capture region from an uncontaminated pion beam which produced approximately uniform captures in the depth interval from 12.5 to 17.5 cm and in the radial interval from 0 to 2.5 cm.*

The effect of incident electrons and muons on the measured cell survival is not available from the experiment. Calculations using the experimental beam cannot be made because the momentum distribution of the beam was not measured. Therefore, to estimate the influence of beam contamination on the comparison, the calculated results are modified in an approximate manner to include contamination. In the calculations of Curtis and Raju[25] in which a beam with the same contamination (35% muons and electrons) as that used in the Raju *et al.* experiment was considered, incident muons and electrons account for 14% of the dose at the depth where the total dose is a maximum. In the calculations of Armstrong and Chandler[10] using a pion beam composed of 29% electrons and muons, 12% of the peak dose is due to the contaminants. By using the depth-dose distribution measured by Raju *et al.*,[24] estimating the dose contribution in the plateau for 35% electron and muon contamination, and assuming that the magnitude of the muon and electron dose is the same at the depth where the pions stop as in the plateau, 18% of the peak dose is due to incident muons

---

*The spatial dependence of the cell-survival probability, OER, and RBE for this beam is given in ref. 7.

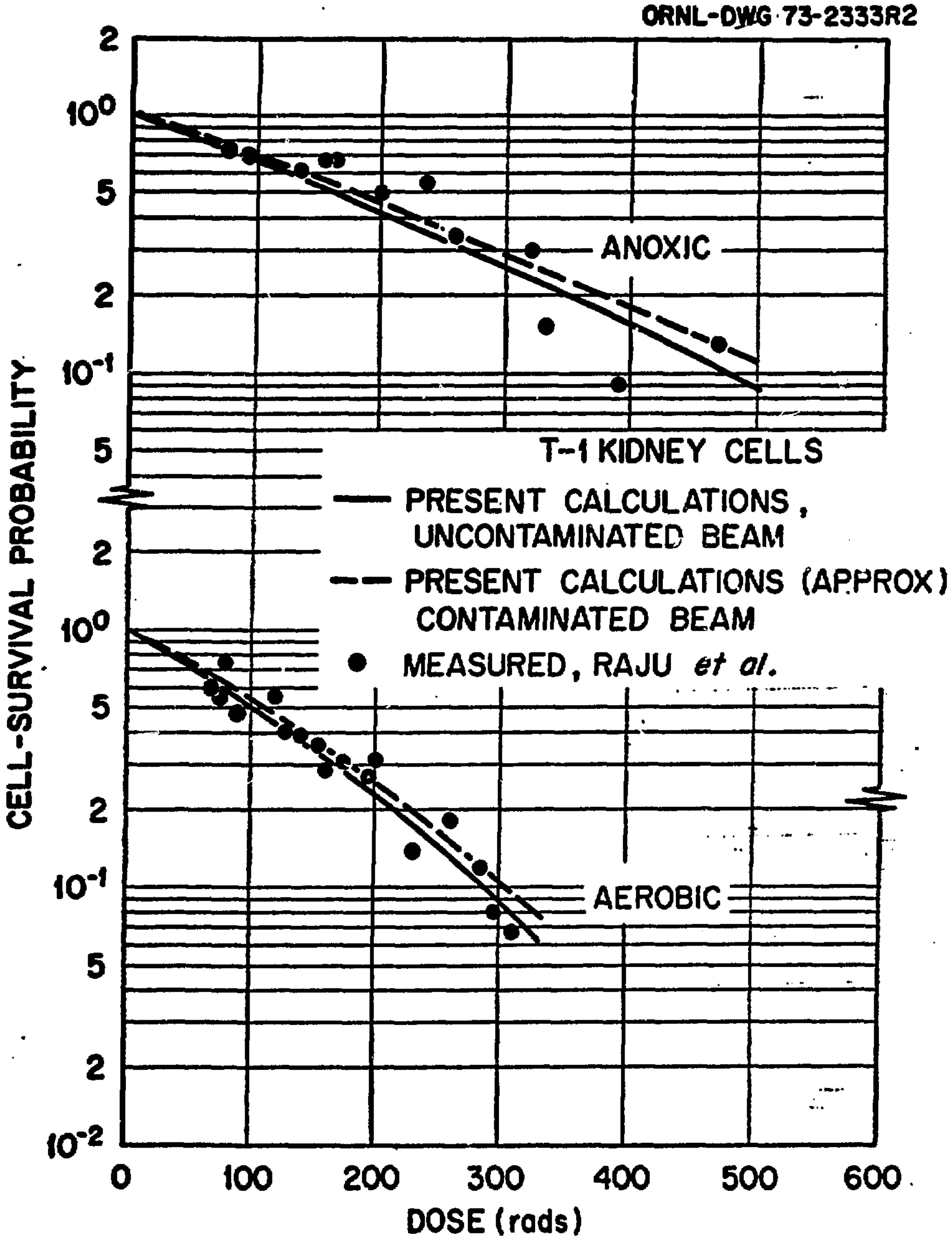

Fig. 5. Comparison of calculated and experimental cell-survival probabilities in the capture region from an incident negatively charged pion beam. Calculated results are given for both a contaminated and an uncontaminated beam.

and electrons. Therefore, a value of 15% was taken as being a reasonable estimate for the contribution of incident muons and electrons to the absorbed dose at the depth at which the cell-survival measurements of Raju *et al.* were made. To estimate the effect that contamination would have on the calculated cell survival, the absorbed dose was increased in the capture region by 15%, and it was assumed that all of the added dose was deposited at very low LET. As shown in Fig. 5, the contamination has a relatively small effect on the cell survival in the capture region.

Another factor that could influence the comparison between the calculated and measured cell survival is the relative amount of dose deposited by pion ionization in the two cases. The fraction of the dose deposited by pion ionization in the capture region is dependent upon position in the capture region and the momentum distribution of the beam. From the calculations of Curtis and Raju[25] where a beam similar to that used in the experiment was considered, 35% of the dose at a depth corresponding to the peak dose is due to primary ionization. For the calculations here, the average contribution to the dose by pion ionization (with contamination) over the volume used in obtaining the cell survival shown in Fig. 5 is also 35%. Thus, while the calculated and experimental cell-survival probabilities shown in Fig. 5 are for different beams, it appears that the conditions in the capture region are sufficiently similar in the two cases to permit a valid comparison.

V. COMPARISON OF ABSORBED DOSES, LET SPECTRA, CELL-SURVIVAL PROBABILITIES, OER's, AND RBE's FOR VARIOUS PARTICLES INCIDENT ON A TISSUE PHANTOM*

The particles considered in this section are ^{60}Co photons, 15-MeV neutrons, neutrons from 35-MeV ^{2}H on Be, negatively charged pions, protons, and alpha particles. The geometry considered is shown schematically in Fig. 6. The upper part of the figure gives the geometry used for photons and neutrons, and the lower part of the figure gives the geometry used for charged particles. The tissue phantom is taken to be 30 cm thick and to be infinite in all directions perpendicular to the axis of the cylindrical symmetry shown in the figure. The composition of the tissue is the same as that used in refs. 4, 5, 7, and 8. The transport calculations for ^{60}Co photons were carried out with the code OGRE-G.[26]

For both photons and neutrons, a point source at a "source-to-skin" distance, d_S, is assumed. For ^{60}Co photons, d_S = 80 cm, for 15-MeV neutrons d_S = 100 cm, and for neutrons from 35-MeV ^{2}H on Be d_S = 125 cm. For both photons and neutrons, the tangent of the angle θ_S is defined to be

$$\tan \theta_S = \frac{1\ \text{cm}}{d_S + 15\ \text{cm}} .$$

For polar angles with respect to the axis of symmetry less than θ_S, the sources are assumed to emit isotropically, and for polar angles greater than θ_S all of the particles emitted by the sources are assumed to be completely removed by a collimator which is not shown in Fig. 6. These conditions correspond at least approximately to those appropriate for the irradiation of a cylindrical region 1 cm in radius at a mean depth of 15 cm in the phantom. The neutron beams incident on the phantom are

---

*Work performed by R. G. Alsmiller, Jr., R. T. Santoro, T. W. Armstrong, J. Barish, K. C. Chandler, and G. T. Chapman.

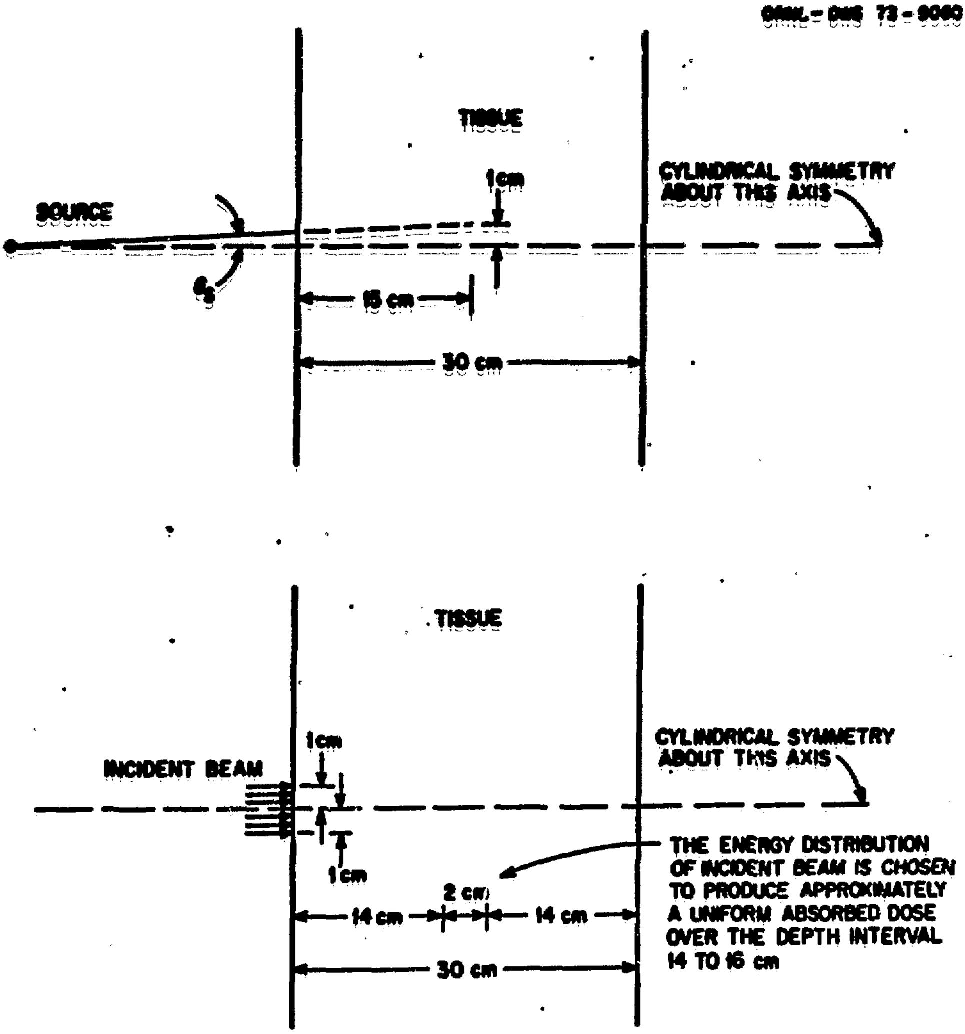

Fig. 6. Schematic diagram of geometry used in the calculations. The upper part of the figure shows the geometry used for photons and neutrons. The lower portion of the figure shows the geometry used for negatively charged pions, protons, and alpha particles. (Note that the drawing is not to scale.)

assumed to be free of photon contamination. The energy distribution of neutrons used in the calculations to represent the neutron spectrum produced by 35-MeV ^{2}H on Be is that shown in Fig. 1.

In the case of pions, protons, and alpha particles, the incident particles are assumed to be normally incident on the phantom. In all cases, the incident beams are taken to be uniform over a circular area of 1-cm radius and to be zero outside of this area. This is significant because the results indicate that for negatively charged pions a 1-cm-radius beam is not the optimum choice for irradiating a region of 1-cm radius at a depth of 15 cm in the phantom. It is assumed that the incident charged-particle beams are free of contamination. The energy distributions of the incident proton, alpha-particle, and pion beams were determined to be those that would produce approximately a uniform absorbed dose over the region of 14 to 16 cm in the tissue phantom. The numerical procedure used to produce these energy distributions is described in ref. 8 and the energy distributions used are shown in Fig. 7. The very rapid increase in the distributions at the higher energies is necessary to keep the absorbed dose uniform at depths which are beyond the ranges of most of the incident particles.

The absorbed doses from ^{60}Co photons, 15-MeV neutrons, and neutrons from 35-MeV ^{2}H on Be are shown in Fig. 8 as a function of depth for several radial intervals. The results shown in the figure for neutrons from 35-MeV ^{2}H on Be are absolute and have units of RAD(INCIDENT NEUTRON)$^{-1}$ when averaged over the specified radial interval (lower two histograms) and

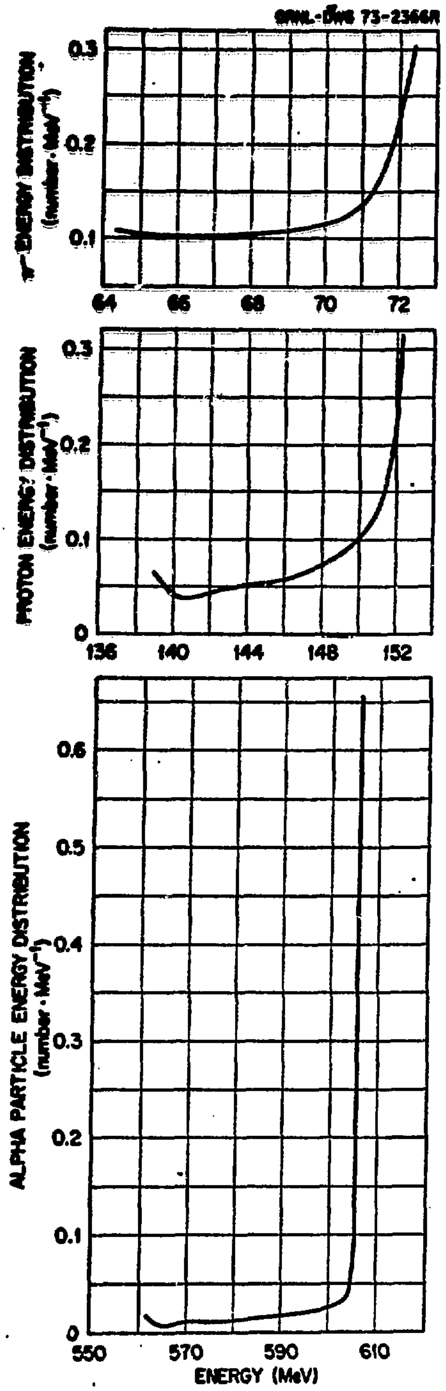

Fig. 7. Energy distribution of incident negatively charged pions, protons, and alpha particles that will produce an absorbed dose that is approximately uniform in the depth interval from 14 to 16 cm. All of the distributions shown have been normalized to unity.

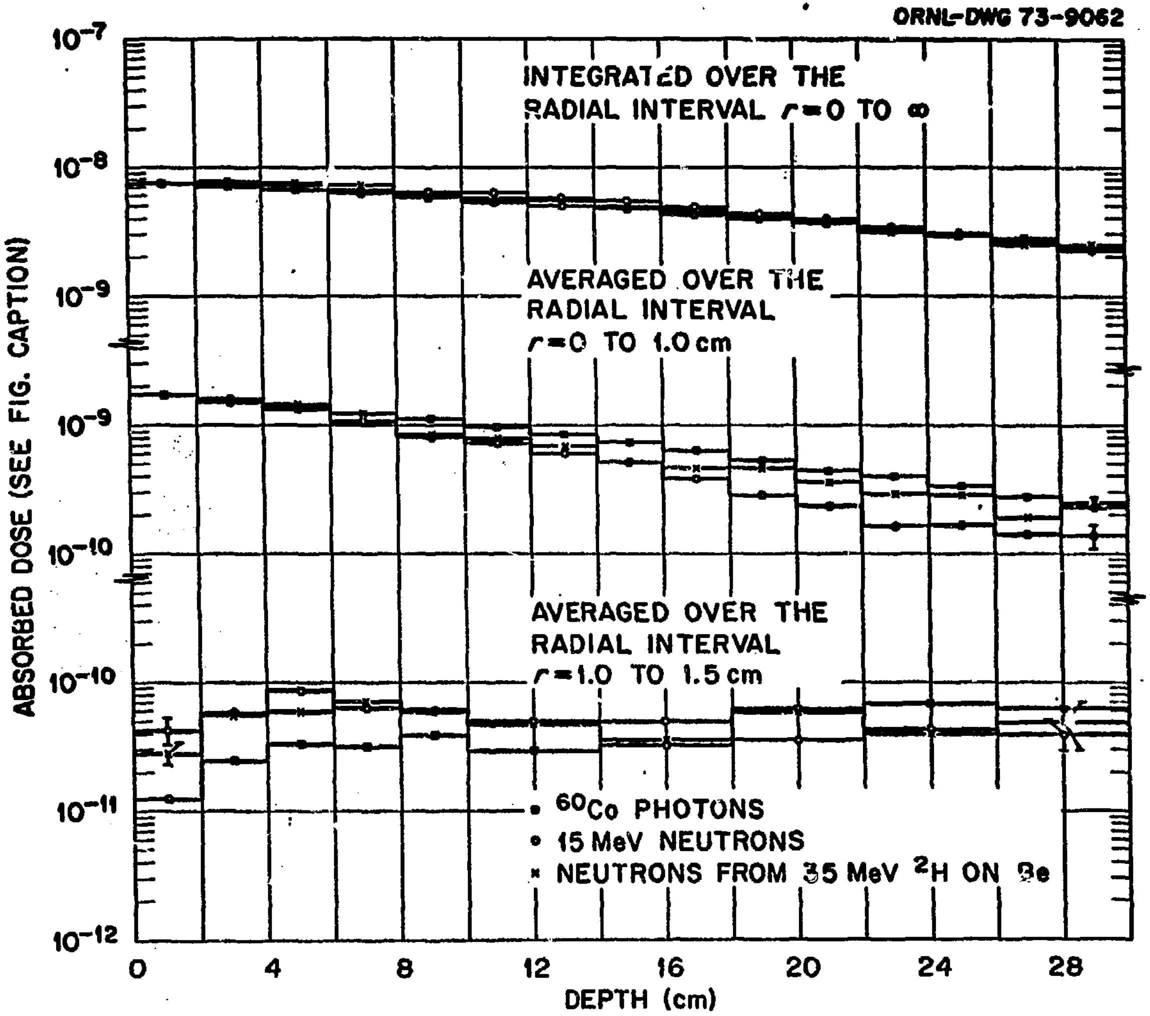

Fig. 8. Absorbed dose vs depth in various radial intervals for incident ^{60}Co photons, 15-MeV neutrons, and neutrons from 35-MeV ^{2}H on Be. The results shown for 35-MeV ^{2}H on Be are absolute with units of RAD(INCIDENT NEUTRON)$^{-1}$ when averaged over the specified radial interval (lower two histogram sets) and RAD CM^2(INCIDENT NEUTRON)$^{-1}$ when integrated over the radial interval from 0 to ∞. For comparison purposes, the results for incident ^{60}Co photons and 15-MeV neutrons have been normalized to agree with the absorbed dose from 35-MeV ^{2}H on Be as explained in the text.

RAD CM^2(INCIDENT NEUTRON)$^{-1}$ when integrated over the radial interval of 0 to infinity.

For comparison purposes, the results for ^{60}Co photons and for 15-MeV neutrons have been normalized to agree with those for neutrons from 35-MeV ^{2}H on Be. The normalization factors used, however, are not the same for the lower two sets of histograms in the figure as for the top set of histograms. For the radial intervals of 0 to 1 cm and 1 to 1.5 cm, the absorbed doses for ^{60}Co photons and for 15-MeV neutrons have been made to agree with the absorbed dose from 35-MeV ^{2}H on Be in the depth interval of 0 to 2 cm and the radial interval of 0 to 1 cm. For the lower two sets of histograms in the figure, absolute values with units of RAD(INCIDENT PHOTON)$^{-1}$ for ^{60}Co photons may be obtained by multiplying the values shown by the factor 0.10, and absolute values with units of RAD(INCIDENT NEUTRON)$^{-1}$ for 15-MeV neutrons may be obtained by multiplying the values given by the factor 0.90.

For the top set of histograms in the figure, the results for ^{60}Co photons and 15-MeV neutrons have been normalized to agree with those for neutrons from 35-MeV ^{2}H on Be in the depth interval of 0 to 2 cm and integrated over all radii. Absolute values with units of RAD CM^2(INCIDENT PHOTON)$^{-1}$ for ^{60}Co photons may be obtained by multiplying the results given in the figure (top set of histograms) by the factor 0.083. Absolute values with units of RAD CM^2(INCIDENT NEUTRON)$^{-1}$ for 15-MeV neutrons may be obtained by multiplying the results given in the figure (top set of histograms) by the factor 1.1.

In Fig. 8 and elsewhere in this report, the error bars are statistical and represent one standard deviation. In Fig. 8 only a few of the error bars are shown. The other error bars are comparable to or less than the error bars which are shown. In the case of incident ^{60}Co photons, the statistical errors are generally smaller than the plotted points.

In the radial interval from 0 to 1.0 cm, the absorbed dose from incident ^{60}Co photons attenuates considerably more slowly with depth than does the absorbed dose from incident 15-MeV neutrons and somewhat more slowly than does the absorbed dose from incident neutrons produced by 35-MeV ^{2}H on Be. In the radial interval from 1.0 to 1.5 cm, the absorbed doses due to both neutron spectra considered are larger than the absorbed doses due to incident photons at the smaller depths, but at the larger depths the absorbed doses due to both incident neutron spectra and to incident photons are comparable within the statistical accuracy of the calculations. It should be noted that at the larger depths in the radial interval of 1.0 to 1.5 cm all of the absorbed-dose histograms in Fig. 8 become relatively constant. This is probably due to the fact that at depths greater than 15 cm in the geometry considered here (see Fig. 6) uncollided particles from the source enter the radial interval of 1.0 to 1.5 cm. The results shown in the lower two histogram sets in Fig. 8 are very dependent upon the geometry considered. The attenuation with depth of the absorbed doses integrated over all radii for the incident ^{60}Co photons and the two incident neutron spectra are shown at the top of Fig. 8. Within the statistical accuracy of the calculations, all three histograms have the same attenuation with depth. This attenuation corresponds approximately to that which might be expected near the center of very broad beams of incident ^{60}Co photons, 15-MeV neutrons, and neutrons from 35-MeV ^{2}H on Be.

The absorbed doses from incident negatively charged pions, protons, and alpha particles are shown in Fig. 9 as a function of depth for several radial intervals. The results for pions given in the figure are absolute with units of RAD(INCIDENT PION)$^{-1}$. For comparison purposes, the absorbed doses for incident protons and alpha particles have been normalized to agree with the absorbed dose from incident pions in the depth interval of 0 to 1.0 cm and the radial interval of 0 to 1.0 cm. Absolute absorbed doses for incident protons in units of RAD(INCIDENT PROTON)$^{-1}$ may be obtained by multiplying the values given in the figure by the factor 1.8. Absolute absorbed doses for incident alpha particles in units of RAD(INCIDENT ALPHA PARTICLE)$^{-1}$ may be obtained by multiplying the values given in the figure by the factor 6.9.

In the radial interval of 0 to 1.0 cm, the absorbed doses from incident protons and alpha particles are comparable, for the normalization used, at depths of less than approximately 16 cm and are very approximately uniform in the depth interval of 14 to 16 cm. At depths greater than 16 cm, the absorbed doses decrease very rapidly. The absorbed doses from incident protons at depths greater than 18 cm become so small that they are not statistically significant and are not shown in the figure. For both incident protons and alpha particles, the ratio of the peak absorbed dose to the surface absorbed dose in the radial interval of 0 to 1.0 cm is approximately 2.

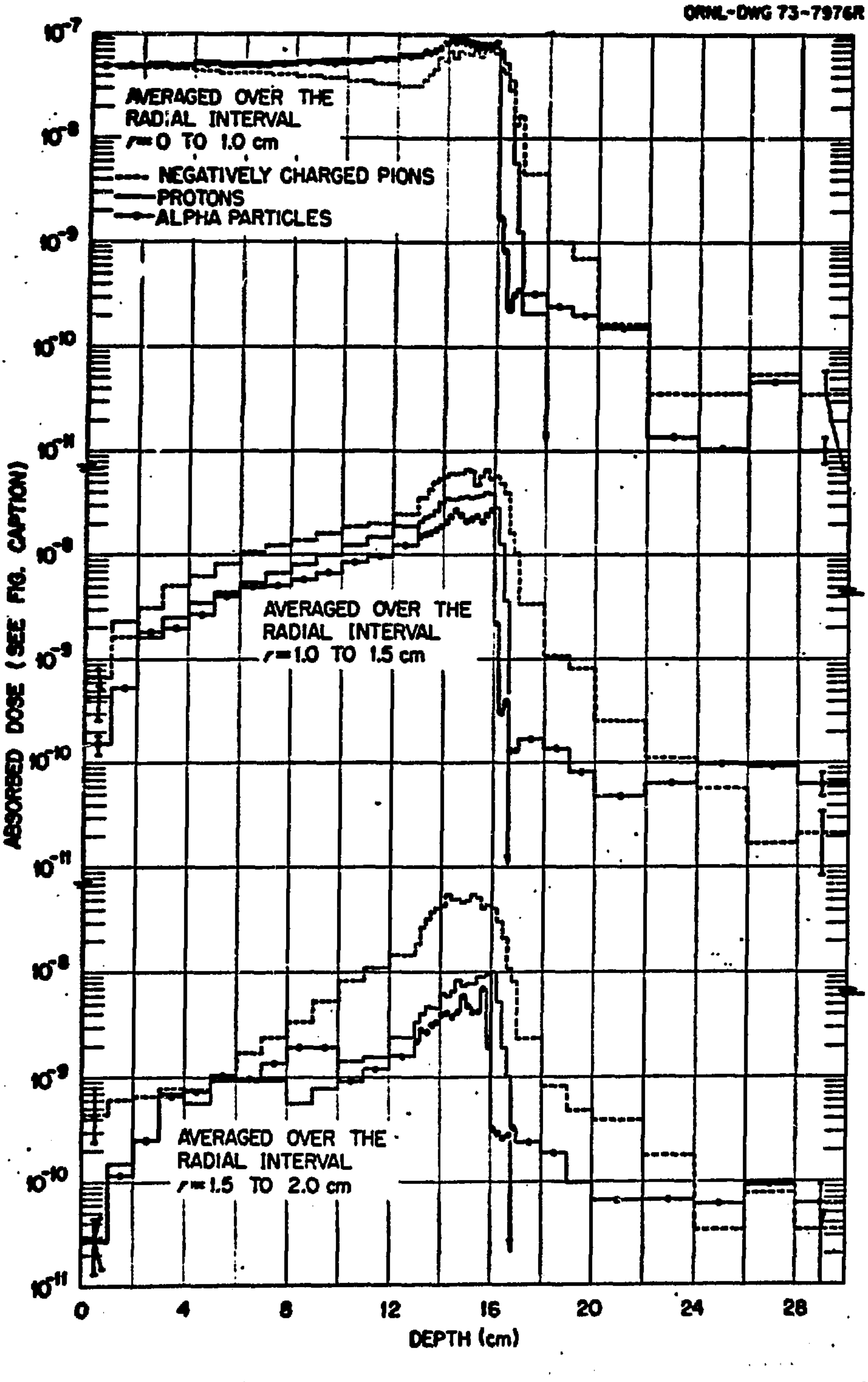

Fig. 9. Absorbed dose vs depth in various radial intervals for incident negatively charged pions, protons, and alpha particles. The results shown for incident pions are absolute with units of RAD(INCIDENT PION)$^{-1}$ when averaged over the indicated radial intervals. For comparison purposes, the results for incident protons and alpha particles have been normalized to agree with the absorbed dose for incident pions in the depth interval of 0 to 1 cm and in the radial interval of 0 to 1 cm. The normalization factors used are given in the text.

The absorbed dose from incident pions in the radial interval of 0 to 1.0 cm decreases as the depth increases from the surface, has a local minimum at a depth of 12 to 13 cm, is approximately uniform in the 14- to 16-cm depth interval, and decreases very rapidly at the larger depths. The ratio of the peak absorbed dose to the surface absorbed dose in this radial interval is approximately 1.4. That the value is less for incident pions than for incident protons or alpha particles is due primarily to the fact that a 1-cm-radius beam has been used for all charged particles and that the multiple Coulomb scattering of pions is larger than that for protons or alpha particles; that is, pions are being lost from the 0- to 1-cm radial interval to a greater extent than either protons or alpha particles due to multiple Coulomb scattering.

In the radial intervals of 1.0 to 1.5 cm and 1.5 to 2.0 cm at depths of less than 16 cm, the absorbed dose from incident pions is somewhat larger than is the absorbed dose from incident protons, and the absorbed dose from incident protons is somewhat larger than is the absorbed dose from incident alpha particles. To a considerable extent, this is due to the differences in the magnitude of multiple Coulomb scattering for the various types of particles, but it also reflects the manner in which energy is deposited by the nuclear-reaction products produced by the various particles. Since multiple Coulomb scattering is very significant in determining the results shown in Fig. 9, particularly for incident pions, it should be clear that the results shown could be changed appreciably by a different choice of radii for the incident beams considered.

The absorbed doses as a function of LET averaged over the depth interval of 14 to 16 cm and the radial interval of 0 to 1 cm are shown in Fig. 10 for incident neutrons, pions, protons, and alpha particles. The LET scale in Fig. 10 begins at $L_{MIN} = 31.6$ MeV cm^{-1}, and it is assumed that photons deposit all of their energy below this L value, so no results are given in the figure for incident ^{60}Co photons.

In Fig. 10 the shape of the LET spectrum for incident pions is considerably different from those for incident protons and alpha particles. The spectrum from incident pions is very approximately uniform over much of the LET range but does show a marked reduction at LET values of $\gtrsim 2 \times 10^3$ MeV cm^{-1}. In this figure, the LET spectra from both incident neutron spectra considered are comparable over much of the LET range but, again, show significant differences at both low and high LET. It is interesting to note that in the 14- to 16-MeV region the shapes of the LET spectra from both incident spectra considered are more nearly comparable to that for incident pions than those for incident protons and alpha particles.

All of the cell-survival results presented here are for T-1 kidney cells and were obtained using the cell-inactivation model of Katz *et al.*[14-16] in the manner described in ref. 7. The cell-survival probability for aerobic T-1 kidney cells is shown in Fig. 11 as a function of depth for two radial intervals for incident ^{60}Co photons, 15-MeV neutrons, and neutrons from 35-MeV ^{2}H on Be. The cell-survival probability in the depth interval of 0 to 2 cm and in the radial interval of 0 to 1 cm has been taken to be 0.30 for the aerobic case for all incident particles. The

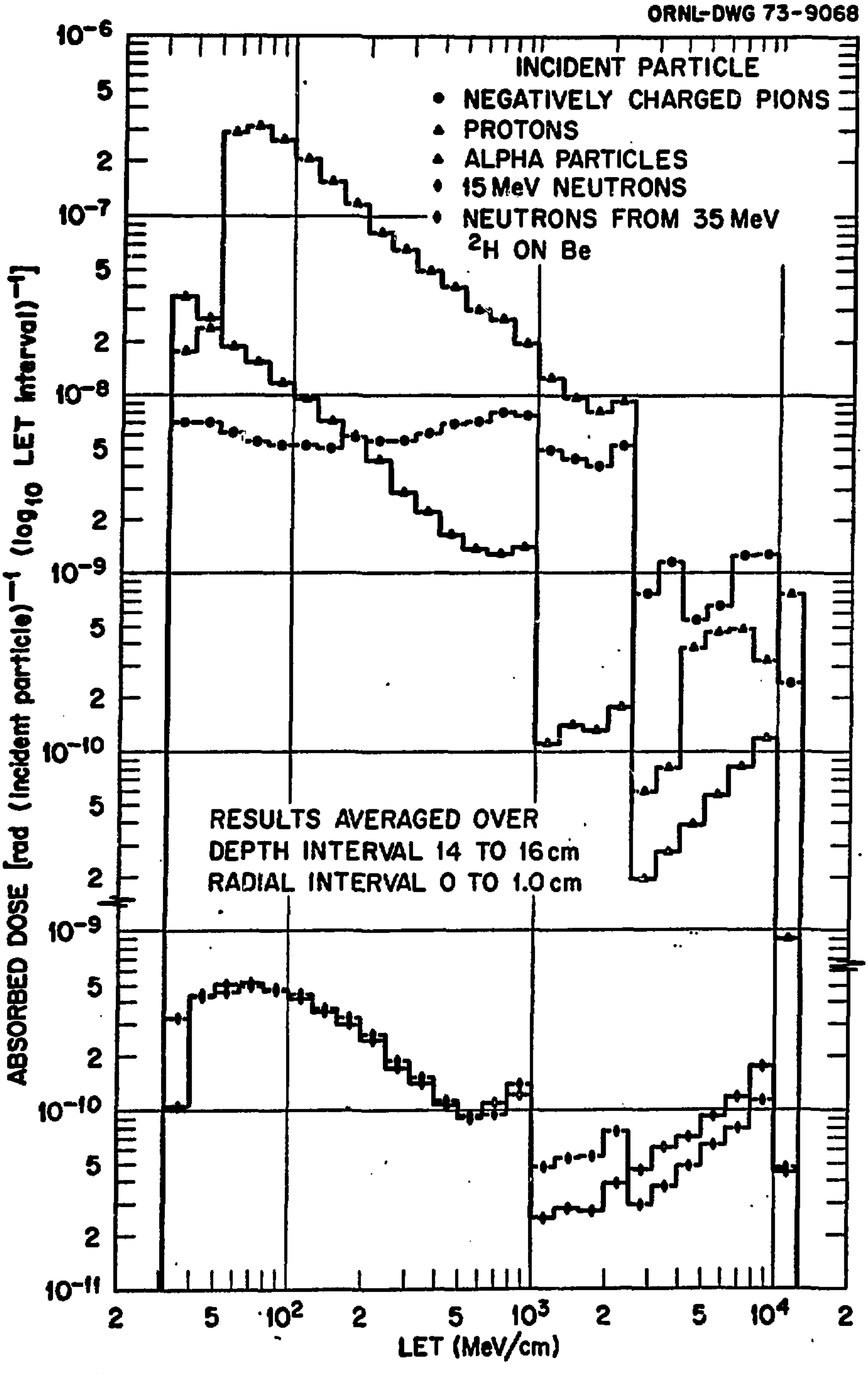

Fig. 10. Absorbed dose vs LET for various incident particles. The results shown are averaged over the depth interval of 14 to 16 cm and the radial interval of 0 to 1 cm.

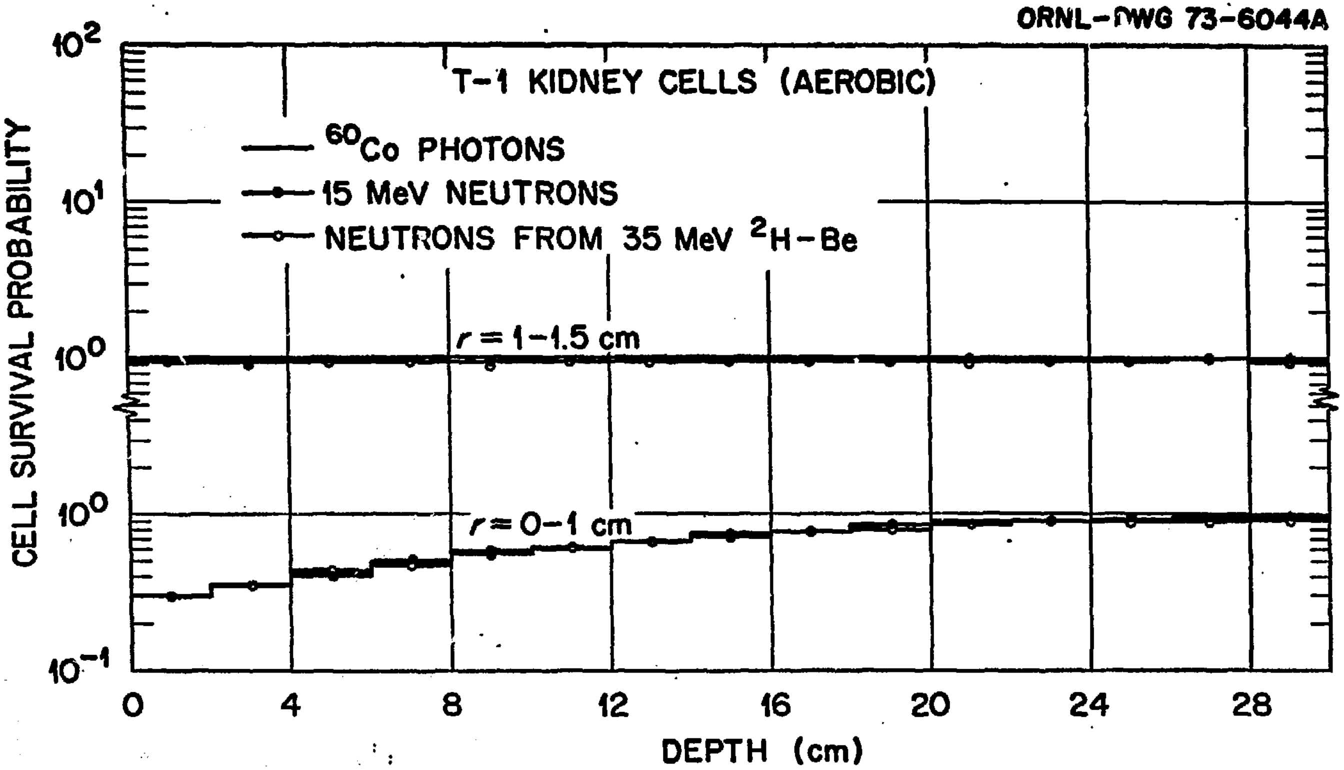

Fig. 11. Cell-survival probability for aerobic T-1 kidney cells vs depth in two radial intervals for incident ^{60}Co photons, 15-MeV neutrons, and neutrons from 35-MeV ^{2}H on Be. The cell-survival probability is taken to be 0.30 in the depth interval of 0 to 2.0 cm and in the radial interval of 0 to 1.0 cm for all incident particles.

absorbed doses in this volume element needed to produce this cell survival are 334 rad for incident ^{60}Co photons, 144 rad for incident 15-MeV neutrons, and 126 rad for incident neutrons from 35-MeV ^{2}H on Be.

In Fig. 11 in the radial interval of 0 to 1 cm, there is no statistically significant difference in the cell-survival probability at any depth for the incident particles considered. The cell-survival probability in the interval of 1.0 to 1.5 cm for all particles considered is nearly unity.

In Fig. 12 the cell-survival probability for aerobic T-1 kidney cells is shown as a function of depth for several radial intervals for incident negatively charged pions, protons, and alpha particles. The cell-survival probability in the depth interval of 0 to 1.0 cm and the radial interval of 0 to 1.0 cm has been taken to be 0.30 for the aerobic case for all incident particles. The absorbed-dose values in this volume element needed to produce this cell-survival probability are 335 rad for incident protons, 326 rad for incident alpha particles, and 304 rad for incident pions.

The cell-survival probabilities in Fig. 12 for incident protons and alpha particles are comparable at all depths and for all radii except in the depth interval of 14 to 16 cm and the radial interval of 0 to 1.0 cm. In this figure, the cell-survival probability for incident pions in the radial interval of 0 to 1.0 cm increases with increasing depth until a depth of 13 cm is reached. This increase is correlated with the decrease with depth of the pion dose in the radial interval of 0 to 1.0 cm shown in Fig. 7, and, as explained in the discussion of Fig. 7, it is due to the fact that the pions are being removed from this radial interval by multiple Coulomb scattering. The relatively small cell-survival probability for incident pions in the depth interval of 14 to 16 cm and in the radial intervals

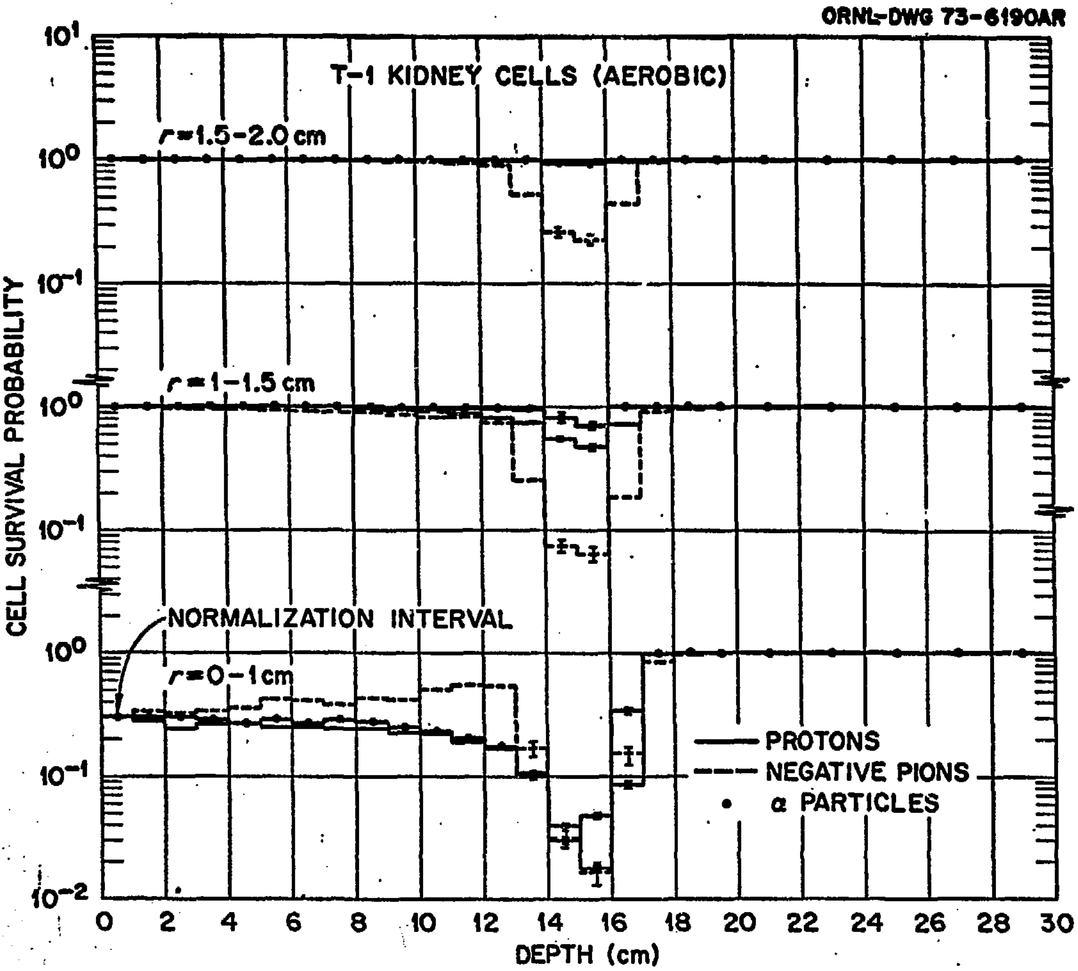

Fig. 12. Cell-survival probability for aerobic T-1 kidney cells vs depth in several radial intervals for incident negatively charged pions, protons, and alpha particles. The cell-survival probability is taken to be 0.30 in the depth interval of 0 to 1.0 cm and in the radial interval of 0 to 1.0 cm for all incident particles.

of 1.0 to 1.5 cm and 1.5 to 2.0 cm is probably also due to multiple Coulomb scattering and to the fact that negatively charged pions deposit a large fraction of their rest energy in the immediate vicinity of the region where they come to rest. In Fig. 12, the cell-survival probabilities for incident pions and alpha particles in the 14- to 16-cm depth interval and the 0- to 1.0-cm radial interval are comparable and are somewhat smaller than those for incident protons. It should be noted that an approximately uniform absorbed dose in the depth interval of 14 to 16 cm (see Fig. 9) does not lead to an approximately uniform cell-survival probability in this depth interval. In Fig. 12, the cell-survival probabilities at depths $\geqslant$ 16 cm very rapidly become unity for all incident charged particles considered.

Cell-survival probabilities averaged over the radial interval of 0 to 1 cm and the depth interval of 14 to 16 cm are shown in Fig. 13 as a function of local dose for all of the incident particles considered. Results are given for both aerobic and anoxic T-1 kidney cells. The abscissa in the figure is labeled "local absorbed dose" to emphasize that the curves give the cell-survival probabilities when the dose values, averaged over the indicated spatial intervals, are the same for all incident-particle types.

In the peak region of the absorbed-dose curves in Fig. 13 for incident charged particles, the cell-survival-probability curves for incident pions are very similar to those for incident neutrons, but for a given local absorbed dose the cell-survival-probability values given by the two incident neutron spectra are somewhat less than the values given by incident pions.

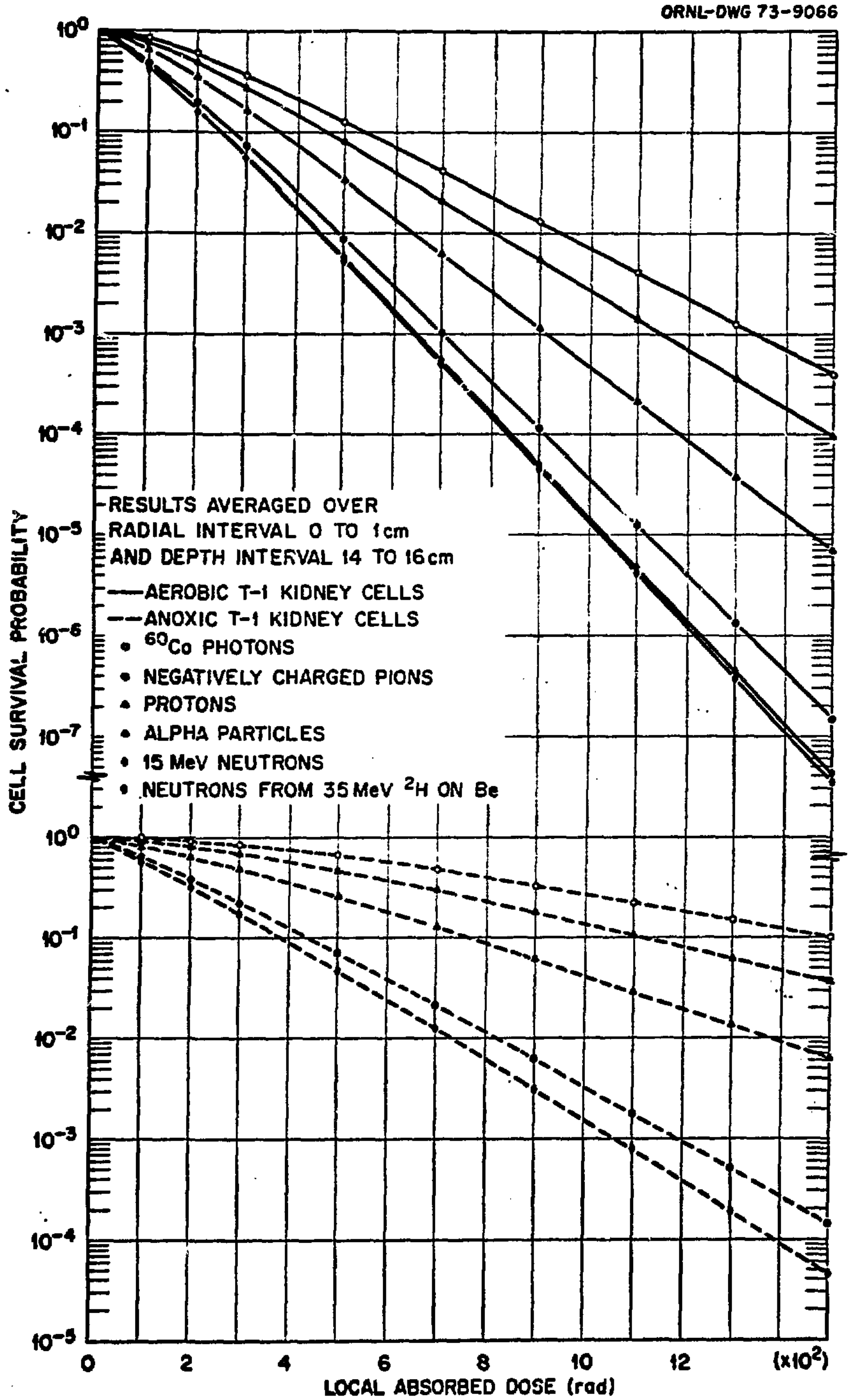

Fig. 13. Cell-survival probabilities for aerobic and anoxic T-1 kidney cells vs local absorbed dose for various incident particles. The results are averaged over the indicated spatial intervals.

From curves such as those shown in Fig. 13, OER and RBE values at a particular survival level in the spatial regions considered and for the particle types considered may be obtained.[7] In Table 1 the OER's at the 10% survival level averaged over several spatial regions are given for all of the incident particle types considered. In the depth interval of 0 to 13 cm and in both radial intervals considered, the OER's for the incident charged particles are slightly less than those for incident photons. In the depth interval of 14 to 16 cm and the radial interval of 0 to 1.0 cm, the OER's for pions are similar to those for neutrons and are smaller than those for incident protons and alpha particles. For both incident neutron spectra considered, the OER's are comparable and are very approximately independent of depth and radius.

In Table 2 the RBE's at the 10% survival level for aerobic T-1 kidney cells averaged over the indicated spatial regions are shown for all of the particles considered. The RBE's for photons are not shown since by definition they are unity. The RBE values show a considerable variation with spatial location and incident particle type.

ORNL-DWG 73-9538

Table 1

OER Values at 10% Survival Level for T-1 Kidney Cells Averaged Over the Indicated Spatial Intervals for Various Incident Particles

Depth Interval (cm)	T-1 Kidney Cells 10% Survival Level					
	Negatively Charged Pions	Protons	Alpha Particles	15-MeV Neutrons	Neutrons from 35-MeV ^{2}H on Be	Photons
			Radial Interval = 0 - 1.0 cm			
0 - 13	2.4	2.6	2.6	1.5	1.5	2.7
14 - 16	1.6	2.4	2.1	1.6	1.6	2.7
17 - 30	1.6	2.2	1.6	1.5	1.6	2.7
			Radial Interval = 1.0 - 1.5 cm			
0 - 13	2.4	2.5	2.5	1.4	1.4	2.7
14 - 16	1.6	2.4	2.1	1.4	1.4	2.7
17 - 30	1.7	2.3	1.9	1.4	1.6	2.7

ORNL-DWG 73-9539

Table 2

RBE Values at 10% Survival Level for Aerobic T-1 Kidney Cells Averaged Over the Indicated Spatial Intervals for Various Incident Particles

Depth Interval (cm)	T-1 Kidney Cells 10% Survival Level for Aerobic Cells				
	Negatively Charged Pions	Protons	Alpha Particles	15-MeV Neutrons	Neutrons from 35-MeV ^{2}H on Be
	Radial Interval = 0 - 1.0 cm				
0 - 13	1.1	1.0	1.1	2.1	2.3
14 - 16	2.0	1.2	1.5	2.2	2.2
17 - 30	2.0	1.3	1.8	2.2	2.1
	Radial Interval = 1.0 - 1.5 cm				
0 - 13	1.1	1.1	1.1	3.4	3.4
14 - 16	2.1	1.2	1.5	3.0	3.3
17 - 30	1.7	1.1	1.4	2.6	2.2

VI. CALCULATIONS RELATED TO THE APPLICATION OF SEMICONDUCTOR DETECTORS IN PION RADIOBIOLOGY*

Initial results have been obtained from calculations directed toward determining the response of silicon detectors placed in the vicinity of a stopped negatively charged pion beam. The main purpose of the calculations is to provide quantitative information to aid in the planning and analysis of radiobiology experiments to be done at the Los Alamos Meson Physics Facility and at the Stanford University Medical Center. Of particular interest is the possibility of inferring the LET distribution of the absorbed dose from the measured pulse-height spectrum.

The case of interest in the calculations to date has been that of a small detector (say, 10 μ to 3 mm thick, 2 to 5 mm in radius) located in a large region of stopping negatively charged pions (Fig. 14). For the initial calculations, a one-dimensional approximation (Fig. 14) has been used with the detector placed at the midpoint of a region 5 cm in width containing a uniform density of π^- captures. The material on either side of the detector was taken to have an approximate tissue composition with the following atom concentrations (in percent): H, 63.3; O, 25.8; C, 9.5; N, 1.4.

The energy deposition in the detector was computed using Monte Carlo methods. First, the position of a π^- capture was selected assuming a uniform spatial distribution of captures within the 5-cm interval. If

---

*This section authored by T. W. Armstrong and K. C. Chandler.

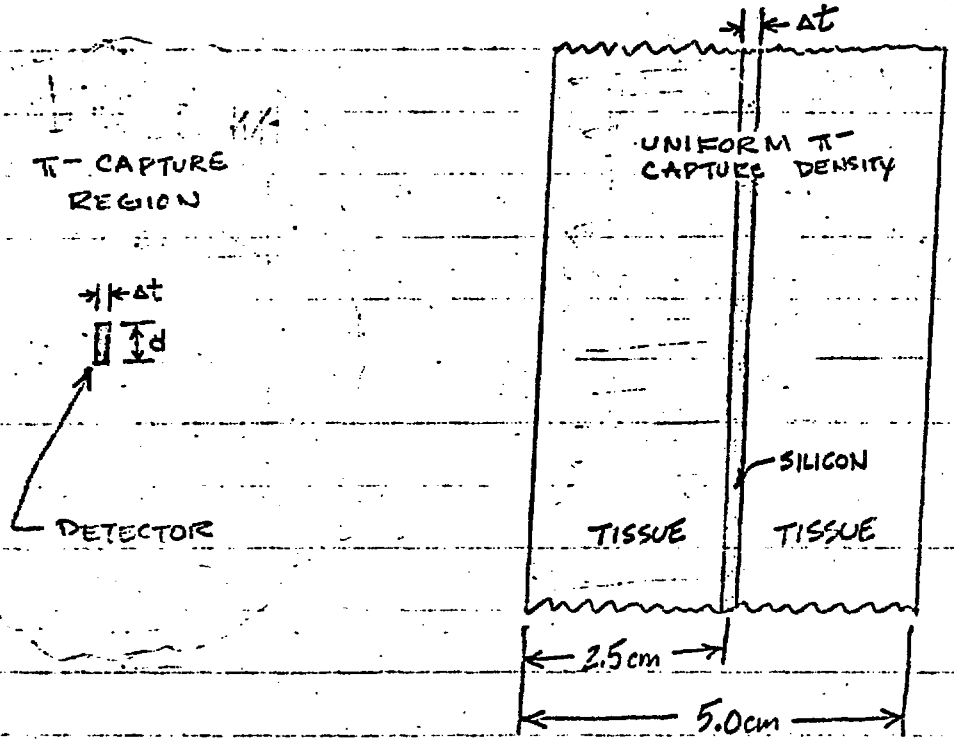

(a)

(b)

Fig. 14. Configuration of interest (a) and one-dimensional approximation used in the calculations (b).

the capture is in the tissue, the type of nucleus (C, N, or O) capturing the pion is determined by using the Fermi-Teller Z-law[27] for the capture probabilities. A Monte Carlo calculation using the intranuclear-cascade-evaporation model[28,29] is then made to obtain the particle type and energy of each of the capture products. Similarly, if the capture takes place inside the detector, an intranuclear-cascade-evaporation calculation is performed for a π^- capture by a silicon nucleus. For each charged-particle product (proton, deuteron, triton, ^{3}He, alpha particle, or residual nucleus), the contribution to the energy deposition in the detector is determined assuming isotropic emission and using ranges and stopping powers generated by the SPAR code[30] (see Fig. 15). For the initial calculations reported here, the energy deposition due to secondary nuclear interactions produced by the π^--capture products, which is expected to be small for the configuration considered, is neglected. It is assumed that the captures result from the slowing down of a parallel beam of pions incident on the left-hand side of the detector. Thus, for each capture occurring inside the detector or in the tissue on the right-hand side of the detector, a contribution to the energy deposition for this capture by the ionization produced by the slowing-down pion is also included (see Fig. 15). It should be noted that by computing the products from each capture separately and by determining the energy deposition from each product separately, correlations resulting from more than one particle per capture contributing to the energy deposition are taken into account properly.

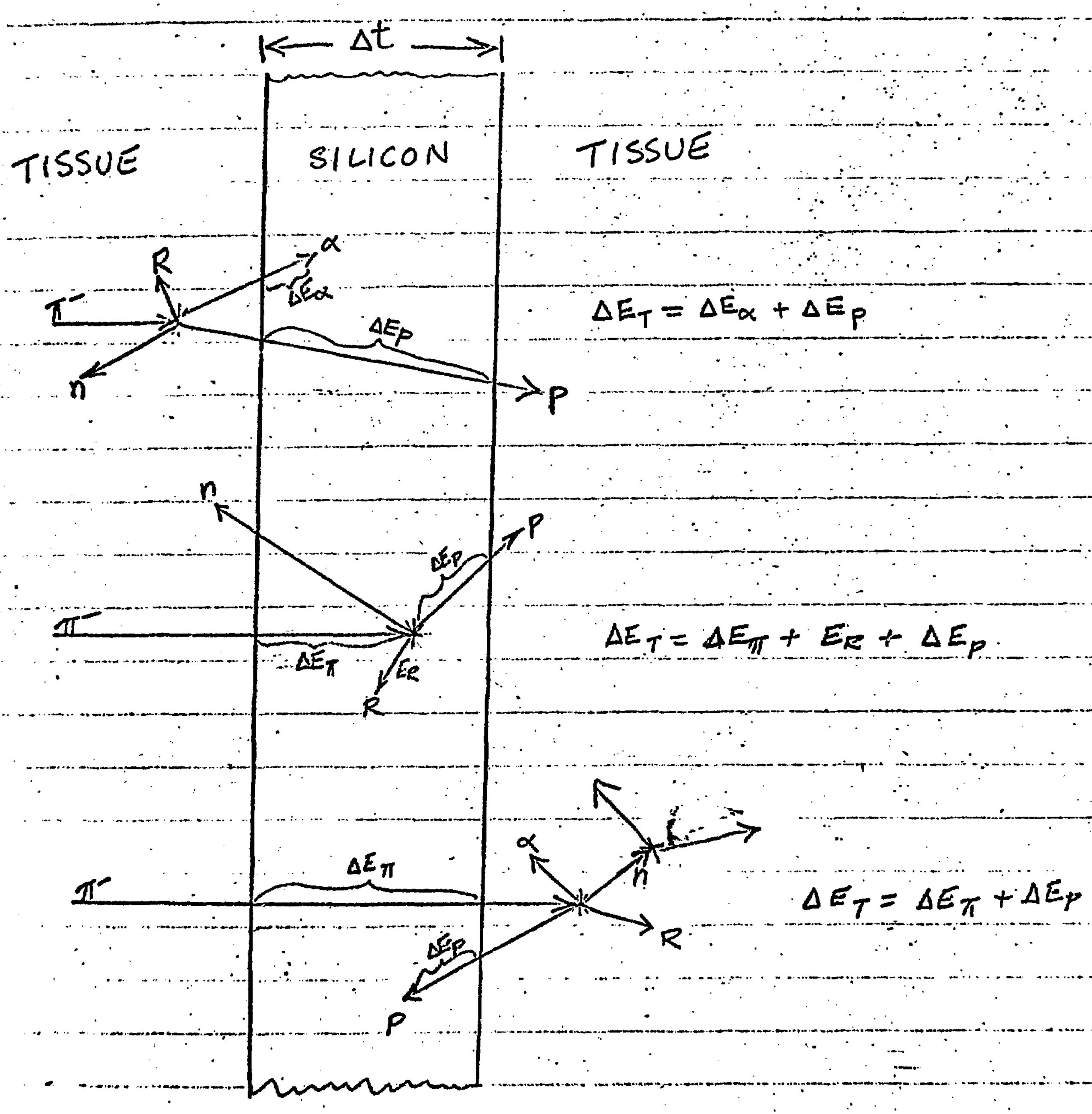

5

Fig 2. Illustration of the procedure for computing the energy deposition in the detector. ΔE_T is the total energy deposition per capture.

Figure 16 shows the calculated energy deposition spectrum (the analogue of a measured pulse-height spectrum) for a 50-μ-thick silicon detector. At a given energy deposition, E, the ordinate of Fig. 16, labeled "frequency," is the number of events (captures) depositing energy in the detector between E and E + ΔE divided by ΔE, the total number of captures, and the detector thickness in g cm^{-2}. The large pion contribution is due to those pions passing through the detector and stopping on the other side. For the configuration chosen, the maximum range of a pion incident on the detector is 2.5 cm in tissue, which corresponds to a kinetic energy of about 24 MeV. Pions at 24 MeV deposit approximately 0.045 MeV in passing through 50 μ of silicon, and these pions produce the maximum in the pion curve shown in Fig. 16. Pions stopping closer to the detector have lower energies, higher stopping powers, and produce larger energy depositions in the detector. The pion curve stops at a maximum energy deposition of 1 MeV, corresponding to the energy of a pion having a range of 50 μ in silicon. Thus, the pion contribution is particularly dependent upon the spatial distribution of the captures and upon the position of the detector within the capture region. With the exception of the maximum in the total spectrum due to passing pions, the contributions of various particle types to the total spectrum overlap to the extent that the total spectrum does not exhibit any prominent changes in shape that can be associated with the contribution of a single type of particle.

Fig 3 16 - Response for a 50 μ silicon detector

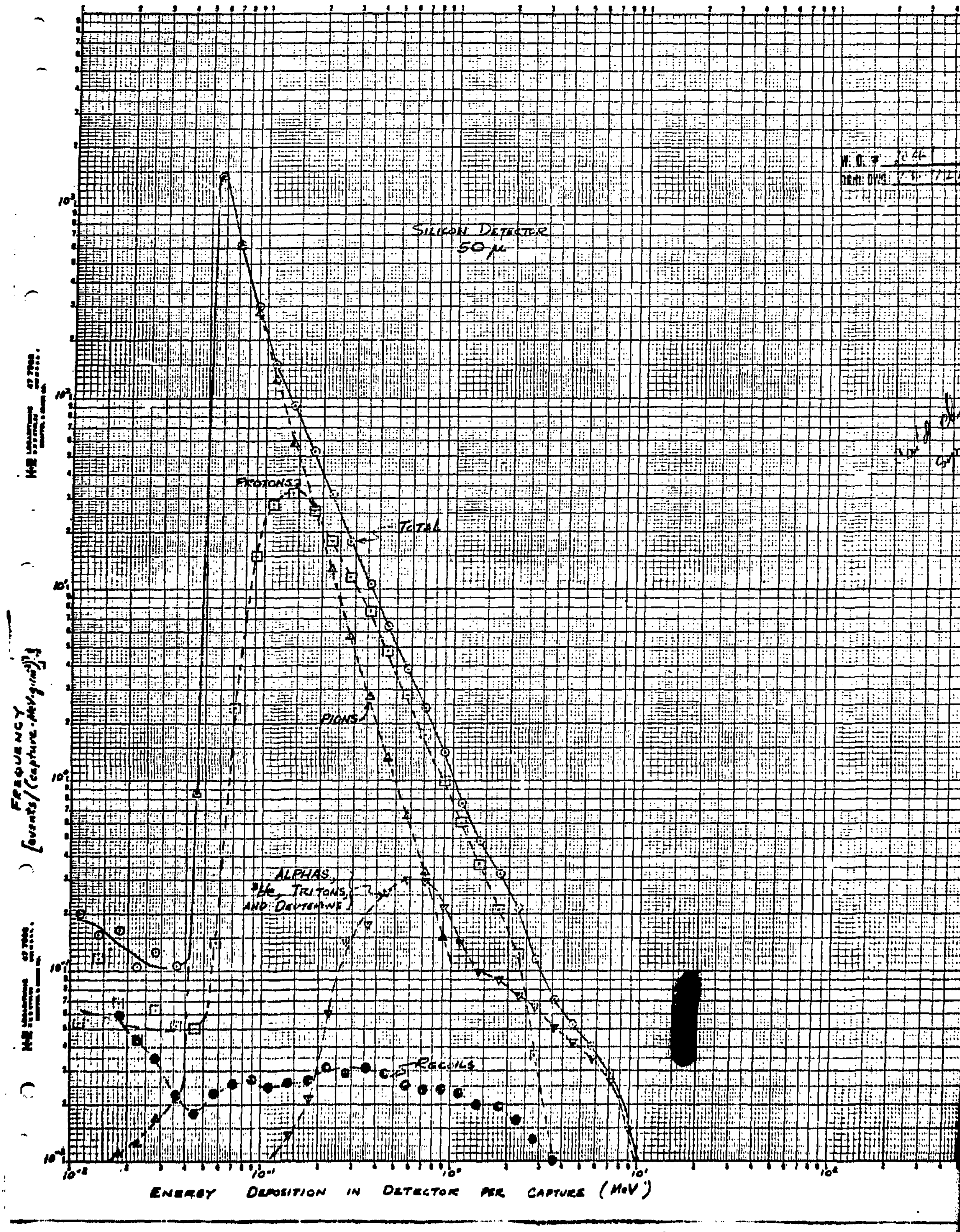

Fig 3/16- Response for a 50μ silicon detector

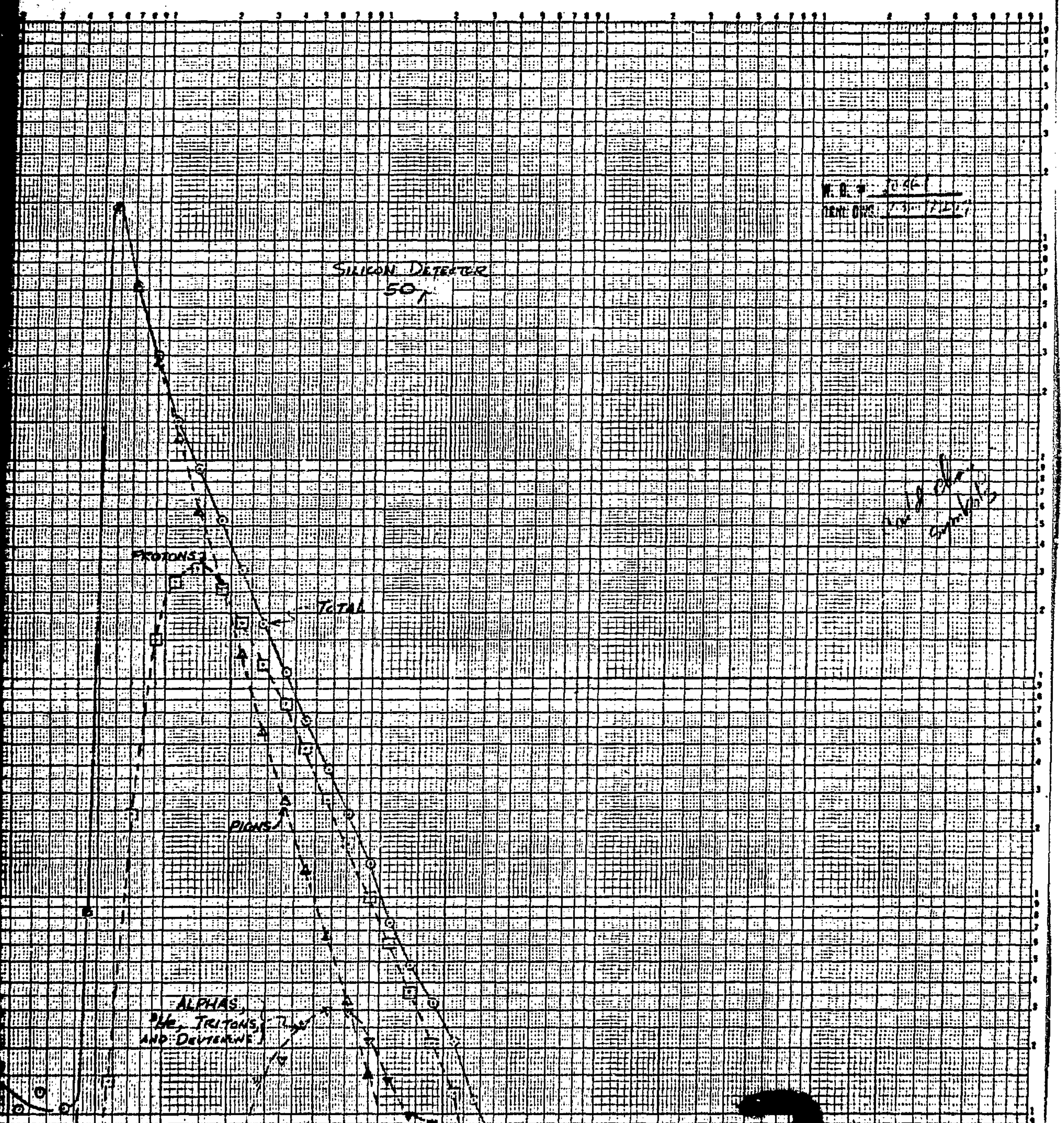

Calculations have also been made to compare the dose that would be measured by the detector to the actual dose in the tissue at the same location. Table 3 shows the total energy deposition (i.e., the frequency spectrum integrated over all energies) for three cases: (a) the energy deposition in a 50-μ-thick silicon detector for the configuration shown in Fig. 14, (b) the energy deposition in 50 μ of tissue at the same location as the detector, and (c) the energy deposition computed with the 50 μ of silicon present and using π^--capture products from silicon if the pions stop in the silicon but using stopping powers and ranges for tissue throughout. In each case, values are given for the energy deposition due to captures occurring at all positions and due only to those captures occurring within the thickness of $\Delta t = 50$ μ. Comparison of cases (a) and (b) shows that the total energy deposition in the silicon is approximately 30% less [8.57 vs 12.4 MeV/(g cm^{-2}) per capture] than in the tissue. Comparison of cases (b) and (c) shows that this difference in energy deposition is due to the differences in stopping powers and ranges for tissue and silicon rather than to differences in the π^--capture products from silicon and tissue. Table 3 also shows that the captures within the detector make only a small contribution (≈ 7%) to the total energy deposition. Thus, a 50-μ silicon detector serves as a probe in the sense that its response is due almost entirely to the π^--capture products produced in the tissue and passing through the detector rather than from capture products within the detector.

ORNL-DWG 73-9537

Table 3

Total Energy Deposition[*]

$\Delta t = 50\ \mu$

Particle Type	Silicon Detector		"Tissue" Detector		Silicon Captures, Tissue Stopping	
	All Captures	Captures in Δt	All Captures	Captures in Δt	All Captures	Captures in Δt
π	3.63	0.05	4.65	0.09	4.65	0.09
p	2.74	0.17	3.67	0.16	3.78	0.27
"α"[†]	1.99	0.21	3.75	0.91	3.23	0.40
Recoils	0.22	0.19	0.35	0.29	0.50	0.44
Total	8.58	0.62	12.4	1.45	12.2	1.2

[*] Values in table correspond to $\Delta E/\Delta t$, where ΔE = energy deposited (MeV) in the detector per π^- capture and Δt = detector thickness in g cm^{-2}.

[†] "α" includes alpha particles, ^{3}He, tritons, and deuterons.

Further calculations are planned to investigate numerous other aspects of the problem - such as the influence of detector thickness and radius, silicon-vs-germanium response, response in the plateau region vs pion-stopping region, and methods for extracting LET information from the pulse-height spectrum.

VII. CALCULATED PARTICLE-PRODUCTION SPECTRA FROM HEAVY ION-NUCLEUS COLLISIONS*†

To study calculationally the use of high-energy heavy ions in cancer radiotherapy, it is necessary to have detailed information on the nuclear-reaction products from the collision of high-energy heavy ions with tissue nuclei. The amount of information needed is so extensive that it is not possible to obtain it experimentally, and therefore a theoretical model to predict it is being developed. The intranuclear-cascade model of nuclear reactions has been shown to reliably predict the nuclear-reaction products from nucleon-nucleus and pion-nucleus collisions,[31-34] so this model is being adapted to the study of heavy ion-nucleus collisions.

The heavy-ion reaction is envisioned to take place as follows: During the passage of the incident heavy ion (projectile) through the target, those nucleons of the projectile that are in the region of overlap undergo quasi-free reactions with the individual nucleons of the target. A cascade is thereby generated simultaneously in both target and projectile. The nucleons that have been jarred free of the binding forces in either the target or projectile and that also manage to survive capture during the development of the cascade escape from the target and projectile. They are emitted as free nucleons in various directions and with a variety of energies. After completion of the cascade, the remaining fragments of the projectile and of the target move off in highly excited states emitting evaporation particles until sufficient excitation energy is lost to stop the evaporation process.

---

*Work performed by H. W. Bertini, T. A. Gabriel, R. T. Santoro, O. W. Hermann, and N. M. Larson.

†Work partially funded by the National Aeronautics and Space Administration under Order H-38280A.

The present version of the heavy-ion-collision model only approximates the feature of the simultaneous cascades in both projectile and target. To this end, we first permit the projectile, moving with velocity $\vec{V}$, to impinge upon a target that is stationary in the laboratory frame of reference. Cascades are allowed to develop only in the target. This is called the "forward" reaction. Then the target, moving with velocity $-\vec{V}$, is made to impinge upon the projectile, which is taken to be stationary, and cascades are then permitted only in the projectile. The directions and energies of all particles thus calculated in this "inverse" reaction are transformed to their corresponding values in the frame of reference of the forward reaction, i.e., in the laboratory frame. The results from the forward and inverse reactions are then each weighted by one-half.

The general physical properties that are simulated for the nuclei of every target and every projectile are as follows: The nucleons making up the nucleus are clustered closer together near the center of the nucleus than on the edges. The density distributions are thus approximations to measured, Fermi-type charge-distribution functions.[35] The outer radius of each nucleus is taken to be that radius at which the measured charge distribution function falls to a fraction of its value at the center. The nucleons bound in the nucleus are in constant motion with zero-temperature, Fermi energy distributions, which are determined by their local densities. Attractive single-particle potentials are assumed to exist in the nucleus, and these are made to vary in strength with the Fermi energy. An approximation to account for exclusion effects in all reactions is incorporated. Further details on the nuclear properties are given in ref. 32, a discussion of the model is given in ref. 17, and a detailed report containing all of the results obtained to date is in preparation.[36]

A comparison between calculated and experimental[37] data for 2.1 GeV per nucleon ^{14}N on ^{12}C is given in Table 4. The results presented are the cross sections for the production of various fragments with velocities between ± 2% and ± 4%* of the incident ion velocity and emitted into the angular interval of 0 to 4 mrad. The agreement between the calculated and experimental data could certainly be better, particularly for the lighter fragments, but there are substantial areas of agreement.

The calculated differential cross section for neutron production from 100 MeV per nucleon ^{12}C collisions with ^{12}C is shown in Fig. 17.[38] It should be noted that at forward angles neutrons are emitted at energies substantially higher than 100 MeV per nucleon. There are no experimental data with which to compare the results, but the data shown are indicative of the kind of data that may be obtained from the model. The power of the model, from the point of view of studying the use of heavy ions in radiotherapy, is that it predicts the energy and angular distributions of all of the particles emitted from a heavy ion-nucleus collision.

---

*The velocity range allowed is not the same for all fragments.

Table 4

Cross Section for the Production of Various Fragments with Velocities Within 2 to 4% of the Incident ^{14}N Velocity and Emitted into the Angular Interval 0-4 mrad from the Interaction of 2.1 GeV/n ^{14}N with ^{12}C

Fragment	Theoretical Results (mb)	Experimental Data[a] (mb)
$^{7}_{3}Li$	0.35 ± 0.18	9.1 ± 3
$^{7}_{4}Be$	0.09 ± 0.09	8.0 ± 1.0
$^{9}_{4}Be$	0.09 ± 0.09	3.0 ± 0.3
$^{8}_{5}B$	0	5.1 ± 0.6
$^{10}_{5}B$	12 ± 1	14.4 ± 2.9
$^{11}_{5}B$	6.5 ± 0.8	10.7 ± 1.3
$^{12}_{5}B$	2.2 ± 0.4	1.9 ± 0.4
$^{9}_{6}C$	0.18 ± 0.12	0.14 ± 0.02
$^{10}_{6}C$	0.35 ± 0.17	0.96 ± 0.12
$^{11}_{6}C$	5.4 ± 0.7	11.3 ± 1.1
$^{12}_{6}C$	58 ± 3	46 ± 9
$^{13}_{6}C$	21 ± 2	9.2 ± 1.8
$^{12}_{7}N$	0.79 ± 0.26	0.63 ± 0.13
$^{13}_{7}N$	11 ± 1	7.7 ± 1.5
Sum	118	128.13
Total Reaction Cross Section	958	
$\% \frac{\text{Sum}}{\text{Total}}$	12%	

[a] H. H. Heckman *et al.*, "Fragmentation of ^{14}N Nuclei at 29 GeV: Inclusive Isotope Spectra at 0°," Phys. Rev. Letters 28, 926 (1972).

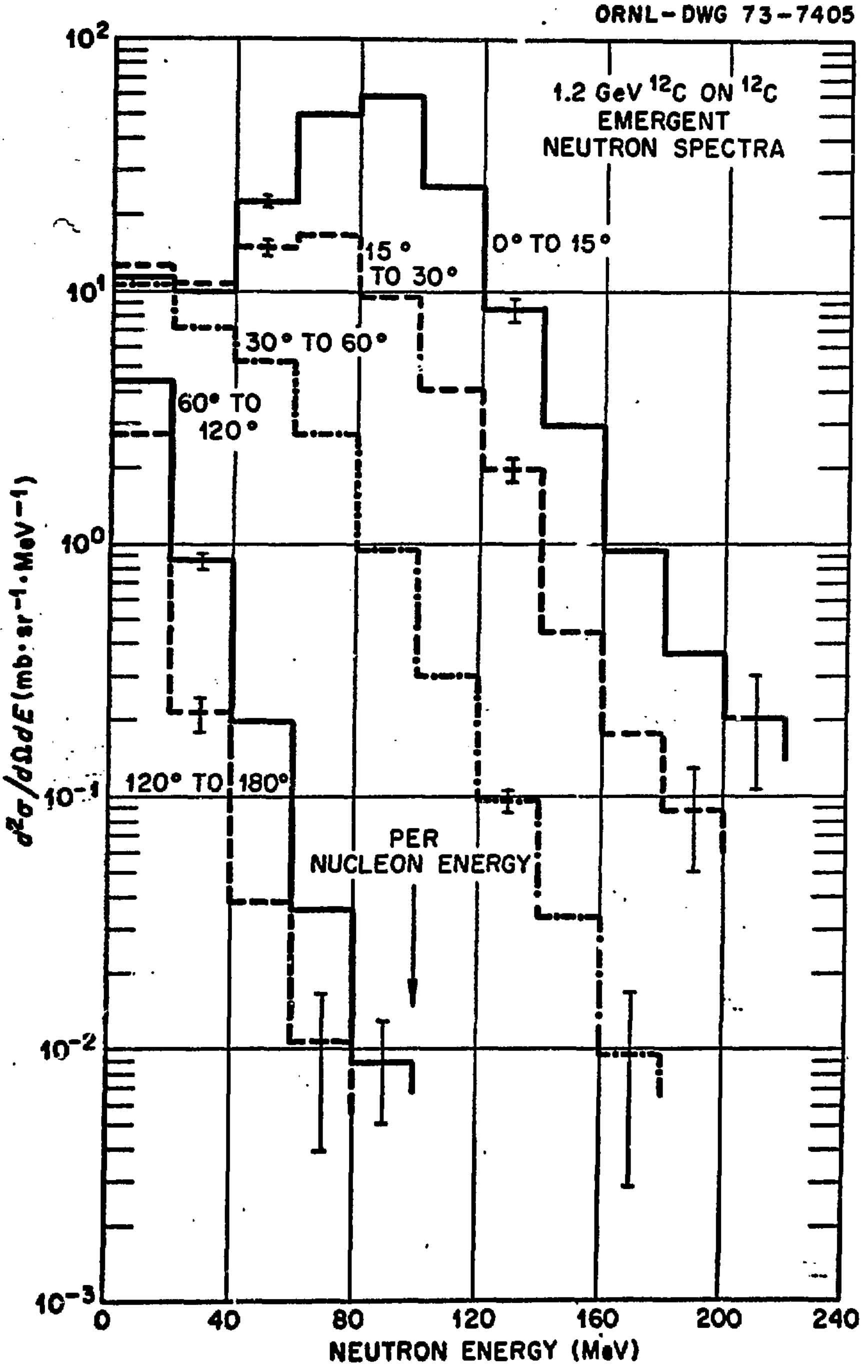

Fig. 17. Differential cross section for the production of neutrons from 100 MeV per nucleon ^{12}C collisions with ^{12}C.

REFERENCES

1. Proc. Conference on Particle Accelerators in Radiation Therapy, October 2-5, 1972, Los Angeles Scientific Laboratory, Los Alamos, New Mexico, LA-5180-C (1973).
2. Progress Report September 1, 1972 - February 28, 1973 on the Research Projects: Calculations for Cancer Radiotherapy with Negatively Charged Pions and A Comparative Study of the Use of Photons, Neutrons, Protons, Negatively Charged Pions, and Heavy Ions in Cancer Radiotherapy, ORNL-TM-4159, Oak Ridge National Laboratory (1973).
3. K. C. Chandler and T. W. Armstrong, Operating Instructions for the High-Energy Nucleon-Meson Transport Code HETC, ORNL-4744, Oak Ridge National Laboratory (1972).
4. R. G. Alsmiller, Jr. and T. W. Armstrong, The Absorbed Dose and Dose Equivalent from Neutrons in the Energy Range 60 to 3000 MeV and Protons in the Energy Range 400 to 3000 MeV, Nucl. Sci. Eng. 42, 367 (1970).
5. R. G. Alsmiller, Jr., T. W. Armstrong, and Barbara L. Bishop, The Absorbed Dose and Dose Equivalent from Negatively and Positively Charged Pions in the Energy Range 10 to 2000 MeV, Nucl. Sci. Eng. 43, 257 (1971).
6. T. W. Armstrong, R. G. Alsmiller, Jr., K. C. Chandler, and B. L. Bishop, Monte Carlo Calculations of High-Energy Nucleon-Meson Cascades and Comparison with Experiment, Nucl. Sci. Eng. 49, 82 (1972).
7. T. W. Armstrong and K. C. Chandler, Calculations Related to the Application of Negatively Charged Pions in Radiotherapy: Absorbed Dose, LET Spectra, and Cell Survival, ORNL-TM-4294, Oak Ridge National Laboratory (1973).

8. T. W. Armstrong, R. G. Alsmiller, Jr., and K. C. Chandler, Calculation of the Dose Induced in Tissue by Negatively Charged Pion Beams, ORNL-TM-4078, Oak Ridge National Laboratory (1973); to be published without appendices in Phys. Med. Biol.

9. T. W. Armstrong and B. L. Bishop, Calculation of the Absorbed Dose and Dose Equivalent Induced by Medium-Energy Neutrons and Protons and Comparison with Experiment, Radiat. Res. 47, 581 (1971).

10. T. W. Armstrong and K. C. Chandler, Monte Carlo Calculations of the Dose Induced by Charged Pions and Comparison with Experiment, Radiat. Res. 52, 247 (1972).

11. T. W. Armstrong, K. C. Chandler, and J. Barish, Calculations of Neutron Flux Spectra Induced in the Earth's Atmosphere by Galactic Cosmic Rays, J. Geophys. Res. 78, 2715 (1973).

12. R. T. Santoro, R. G. Alsmiller, Jr., and K. C. Chandler, Shielding of Manned Space Vehicles Against Galactic Cosmic-Ray Protons and Alpha Particles, Nucl. Sci. Eng. 52, 124 (1973).

13. J. E. Turner *et al.*, The Computation of Pion Depth-Dose Curves in Water and Comparison with Experiment, Radiat. Res. 52, 229 (1972).

14. R. Katz *et al.*, Inactivation of Cells by Heavy Ion Bombardment, Radiat. Res. 47, 402 (1971).

15. R. Katz, S. C. Sharma, and M. Homayoonfar, The Structure of Particle Tracks, Chapter 6, Topics in Radiation Dosimetry, Suppl. 1 to Radiation Dosimetry, Ed. Frank A. Attix, Academic Press, New York, 1972.

16. Robert Katz and S. C. Sharma, Response of Cells to Fast Neutrons, Stopped Pions, and Heavy Ion Beams, preprint (1973).

17. H. W. Bertini, T. A. Gabriel, and R. T. Santoro, Predicted Proton Spectrum at Forward Angles for 29.4-GeV N on C Collisions, ORNL-TM-4311, Oak Ridge National Laboratory (1973).

18. R. B. Theus *et al.*, Neutron Kerma by Time-of-Flight Technique, Appendix v of Middle Atlantic Neutron Therapy Association (MANTA) Progress Report, sub. by C. C. Rogers, M.D., Virginia Commonwealth University, Medical College of Virginia, Richmond, Virginia (1973).

19. Richard B. Theus, Neutron Delivery, Appendix iii (MANTA), op. cit. (1973).

20. Paul Todd *et al.*, Spatial Distribution of Human Cell Lethality in a Neutron Beam Designed for Therapy, Appendix vi (MANTA), op. cit. (1973).

21. R. Katz, S. C. Sharma, and M. Homayoonfar, Detection of Energetic Heavy Ions, Nucl. Instr. Meth. <u>100</u>, 13 (1972).

22. G. W. Barendsen and J. J. Broerse, Dependence of the Oxygen Effect on the Energy of Fast Neutrons, Nature <u>212</u>, 722 (1966).

23. G. W. Barendsen and J. J. Broerse, Measurements of Relative Biological Effectiveness and Oxygen Enhancement Ratio of Fast Neutrons of Different Energies, in Biophysical Aspects of Radiation Quality, IAEA, Vienna (1967).

24. M. R. Raju *et al.*, RBE and OER of π Mesons for Damage to Cultured T-1 Cells of Human Kidney Origin, Brit. J. Radiol. <u>45</u>, 178 (1972).

25. Stanley B. Curtis and Mudundi R. Raju, A Calculation of the Physical Characteristics of Negative Pion Beams - Energy-Loss Distribution and Bragg Curves, Radiat. Res. 34, 239 (1968).

26. D. K. Trubey and M. B. Emmett, OGRE-G, an OGRE System Monte Carlo Code for the Calculation of Gamma-Ray Dose Rate at Arbitrary Points in an Arbitrary Geometry, ORNL-TM-1212, Oak Ridge National Laboratory (1966).

27. E. Fermi and E. Teller, The Capture of Negative Mesotrons in Matter, Phys. Rev. 72, 399 (1947).

28. Hugo W. Bertini and Miriam P. Guthrie, Results from Medium-Energy Intranuclear-Cascade Calculation, Nucl. Phys. A169, 670 (1971).

29. M. P. Guthrie, R. G. Alsmiller, Jr., and H. W. Bertini, Calculation of the Capture of Negative Pions in Light Elements and Comparison with Experiments Pertaining to Cancer Radiotherapy, Nucl. Instr. Meth. 66, 29 (1968); with erratum Nucl. Instr. Meth. 91, 669 (1971).

30. T. W. Armstrong and K. C. Chandler, SPAR, a FORTRAN Program for Computing Stopping Powers and Ranges for Muons, Charged Pions, Protons, and Heavy Ions, ORNL-4869, Oak Ridge National Laboratory (1973).

31. N. Metropolis, R. Bivins, and M. Storm, Monte Carlo Calculations on Intranuclear Cascades. II. High-Energy Studies and Pion Processes, Phys. Rev. 110, 204 (1958).

32. Hugo W. Bertini, Low-Energy Intranuclear Cascade Calculation, Phys. Rev. 131, 1801 (1963); with erratum Phys. Rev. 138, AB2 (1965).

33. Hugo W. Bertini, Intranuclear-Cascade Calculation of the Secondary Nucleon Spectra from Nucleon-Nucleus Interactions in the Energy Range 340 to 2900 MeV and Comparisons with Experiment, Phys. Rev. 188, 1711 (1969).

34. Hugo W. Bertini, Nonelastic Interactions of Nucleons and π Mesons with Complex Nuclei at Energies Below 3 GeV, Phys. Rev. C6, 631 (1972).

35. Robert Hofstadter, Electron Scattering and Nuclear Structure, Rev. Mod. Phys. 28, 214 (1956).

36. H. W. Bertini, T. A. Gabriel, R. T. Santoro, O. W. Hermann, N. M. Larson, and J. D. Hunt, HIC-1, a First Approach to the Calculation of Heavy-Ion Reactions at Energies $\geqslant$ 50 MeV/Nucleon, ORNL-TM-4134, Oak Ridge National Laboratory (in preparation).

37. H. H. Heckman *et al.*, Fragmentation of ^{14}N Nuclei at 29 GeV: Inclusive Isotope Spectra at 0°, Phys. Rev. Letters 28, 926 (1972).

38. T. A. Gabriel, R. T. Santoro, H. W. Bertini, and N. M. Larson, Calculated Secondary-Particle Spectra from Alpha-Particle- and Carbon-Induced Nuclear Reactions, ORNL-TM-4334, Oak Ridge National Laboratory (in press).